U.S. DEPARTMENT OF COMMERCE
NATIONAL OCEANIC AND ATMOSPHERIC ADMINISTRATION
NATIONAL WEATHER SERVICE
NATIONAL METEOROLOGICAL CENTER

OFFICE NOTE 418

CONVECTIVE TRIGGER FUNCTION FOR A MASS-FLUX CUMULUS PARAMETERIZATION SCHEME

Song-You Hong, and Hua-Lu Pan
Environmental Prediction Center

December 1997

Convective Trigger Function for a Mass-Flux Cumulus Parameterization Scheme

Song-You Hong and Hua-Lu Pan

Environmental Modeling Center, National Centers for Environmental Prediction, Washington D.C.

December 1997

(Resubmitted to Mon. Wea. Rev.)

Address for correspondence : Dr. Song-You Hong, GSC/SAIC at NCEP/EMC, Room 207,

5200 Auth Road, Camp Springs, MD 20746, USA.

E-mail : Songyou.Hong@noaa.gov

ABSTRACT

A precipitation physics package for the NCEP Regional Spectral Model designed to improve the skill of precipitation forecasts is proposed. The package incorporates a prognostic grid-resolvable precipitation scheme and a parameterized convection scheme with a convective trigger function that explicitly couples boundary layer and convective precipitation processes. Comprehensive sensitivity experiments were conducted with a grid spacing of approximately 25 km for a heavy rain case over the United States during 15-17 May 1995. In this paper, the trigger function set-up in the convective parameterization scheme and its impact on the predicted precipitation are discussed. Special attention is given to the interaction of cloud properties in the parameterized convection with the evolution of grid-resolvable precipitation physics. The impact of convective forcing due to different convective triggers on the large-scale pattern downstream is also discussed. The implementation of the prognostic cloud scheme and performance are presented in our companion paper (Hong et al. 1998).

1. Introduction

The nested, regional spectral model (RSM) developed by Juang and Kanamitsu(1994) has been used as an experimental model at the National Centers for Environmental Prediction (NCEP) for more than one year. During the cool season, its forecasts of precipitation have proven to be comparable to those of other forecast models, but, during the warm season, it has not been as successful. This performance has been attributed to the fact that the algorithms used for the computation of precipitation were taken directly from the larger scale, global medium-range forecast model (MRF) within which the RSM is nested. The MRF physics algorithms are described in Kanamitsu(1989), Kanamitsu et al.(1991), and their subsequent developments are presented by Pan and Wu(1995), and Hong and Pan(1996).

When a prediction model, such as the RSM, can resolve processes with horizontal scale less than 50 km, the neglect of the storage of water as cloud droplets may become an unnecessary source of error. There is general agreement that models intended for the prediction of mesoscale processes must include at least some explicit treatment of cloud water. In a companion paper (Hong et al. 1998), we have presented evidence that the inclusion of an algorithm that explicitly predicts clouds in the 25 km version of the RSM has a significant, positive impact on the skill of the model's precipitation forecast.

In this paper, we report on tests of a modification of the parameterization of convective precipitation used in the RSM and MRF models. The modification involves the use of a new set of "convective trigger functions" in the terminology of Rogers and Fritsch(1996). As indicated by Kain and Fritsch(1992), Stensrud and Fritsch(1994), and Rogers and Fritsch(1996), the convective trigger function must be recognized as important as parameterized cloud characteristics in the

cumulus parameterization scheme. They showed that the simulations of mesoscale convective systems are quite sensitive to the formulation of the triggering mechanism.

Difficulty arises when grid-resolvable forcing is weak over a broad area where CAPE is relatively large. Under this synoptic situation, an air parcel originating near the surface typically has a negative buoyancy with respect to the environmental sounding. In a composite analysis of data collected during the Preliminary Regional Experiment for STORM-Central (PRE-STORM) period, Zhang and McFarlane(1991) showed that air parcels had minimum buoyancy at their lifting condensation levels (LCL). Emanuel and Raymond(1991) pointed out that one must be able to forecast the local disappearance or reduction of the capping inversion that restrains convection when the initial convection appears in a conditionally unstable atmosphere. Of importance to the cumulus parameterization is the measurement of the subgrid scale forcing required to raise an air parcel up to its LFC. Recently, a general framework for convective trigger functions was proposed by Rogers and Fritsch(1996). Readers are urged to refer to their paper for a comprehensive description about the background of the new trigger. Their concept has been adapted in this study to determine the buoyancy of the parcel due to subgrid scale buoyancy forcing, in conjunction with the large eddy induced turbulence. Thermal excess of the buoyant parcel is used here, while Rogers and Fritsch(1996) originally formulated it based on the vertical velocity perturbations in the Kain and Fritsch(1993) scheme.

A brief review of the RSM is given in section 2. Then in section 3, we present the new set of "convective trigger functions" and discuss their formulation in the context of previous observational and experimental work. An evaluation of the proposed new system is conducted by evaluating the RSM forecasts over a two day period beginning at 1200 UTC 15 May 1995. This

case is described, together with an explanation of out experimental design, in section 4. Results are presented and interpreted in section 5. The paper ends with a summary and concluding remarks.

2. The NCEP RSM

a. General

The NCEP RSM is a primitive equation model using the sigma-vertical coordinate. A detailed description of the model is given by Juang and Kanamitsu(1994). Further developments and applications are available in Juang et al.(1997). The version of the RSM used in this study employs the same "physics package" as the MRF, as documented in Hong and Pan(1996). Both models include long-and short- wave radiation, cloud-radiation interaction, planetary boundary-layer processes, deep and shallow convection, large-scale condensation, gravity wave drag, enhanced topography, simple hydrology, and vertical and horizontal diffusion. Since the surface, boundary-layer, and precipitation physics are very important aspects of the model and have been significantly changed recently, a more detailed description of these parameterizations is given below.

b. Surface layer and boundary-layer physics

The current MRF model utilizes the 2-layer soil model of Mahrt and Pan(1984), Pan and Mahrt(1987) with some modifications based on Pan(1990). The soil model includes soil thermodynamics and soil hydrology, both modeled as a diffusion process. The evaporation process in the surface energy balance is modeled by three components: direct evaporation from the bare

soil surface, transpiration through the leaf stomatae, and evaporation of precipitation intercepted by the leaf canopy.

The boundary layer physics employs a nonlocal diffusion concept developed by Hong and Pan (1996). This scheme is strongly coupled to the surface layer physics. In the scheme, the turbulent diffusivity coefficients are calculated from a prescribed profile shape as a function of boundary-layer height and scale parameters derived from similarity requirements. Above the mixed layer, the local diffusion approach is applied to account for free atmospheric diffusion. Hong and Pan(1996) examined the impacts of tuning the parameters of the scheme on the predicted precipitation and also showed that consistent improvements in the skill of precipitation forecasts could be obtained.

c. Precipitation physics

Precipitation is produced by both large-scale condensation and the convective parameterization schemes. The large-scale precipitation algorithm checks supersaturation in the predicted specific humidity. Latent heat is released as the specific humidity and temperature are adjusted to saturation values. The scheme does not include a prognostic cloud, but evaporation of rain in the unsaturated layers below the level of condensation is taken into account.

The current version of the deep convection scheme (NCEP scheme) follows Pan and Wu (1995), which is based on Arakawa and Schubert(1974), and simplified by Grell (1993) with a saturated downdraft. Recent changes to the scheme are discussed in Hong and Pan (1996). Hong and Pan(1996) improved the scheme to allow convection in disturbed atmospheric conditions to effectively eliminate the convective available potential energy (CAPE). The primary differences between Pan and Wu(1995) and Grell(1993) lie in the closure(the NCEP scheme uses the original Arakawa-Schubert closure) and the treatment of subcloud layers (the NCEP scheme allows

entrainment of updraft and detrainment of downdraft between the updraft-air originating level and the level of free convection (LFC)). In the scheme, mass flux of the cloud is determined using a quasi-equilibrium assumption based on a threshold cloud work function deduced from observations (Lord 1978). The level of maximum moist static energy between the surface and 400 hPa level from the surface is used for an updraft-air originating level. Convection is suppressed when the distance between the updraft-air originating level and the LFC exceeds a certain threshold (currently 150 hPa). The LFC is the cloud base. Cloud top is determined as the first neutral level from the cloud base upward. Cloud depth needs to be deeper than 150 hPa to initiate convection. The cloud work function must be greater than 0, a check on the integrated buoyancy of the cloud.

3. Convective trigger function

According to Rogers and Fritsch(1996), the subgrid scale perturbation contribution terms can be classified as due to surface inhomogeneities, convective turbulence, and clear air turbulence, respectively. Surface inhomogeneities (e.g., compex terrain, land/water interfaces, and vegetation coverage differences) can play a role in triggering convection, especially during the warm-season daytime hours. Due to the lack of an observational database for measures of inhomogeneity, a grid-size dependence to the inhomogeneity spectrum, as in Rogers and Fritsch(1996), was adapted. This approach stems from the recognition that there should be more and larger subgrid-scale features that create inhomogeneities within larger grid elements, and it can be expressed by

$$\theta'_{sfc} = \frac{\theta'_{\max}}{\pi}\left[\tan^{-1}\left\{a\left(\Delta x - \Delta x_0\right)\right\} + \frac{\pi}{2}\right] \qquad (1)$$

where θ'_{max} represents the maximum potential temperature perturbation and is taken as 1K. Letter a stands for the slope coefficient related to grid size dependency and is chosen to be $2\times10^{-5}m^{-1}$. Δx is the horizontal grid size (m) and Δx_0 the reference value of horizontal grid size, which is taken as $3\times10^{4}m$. This formula gives a larger(smaller) value as the horizontal grid size increases (decreases), ranging from, for example, 0.37K at Δx= 10 km to 0.92 K at Δx=230 km. A 230 km resolution corresponds to the spectral truncation of T62 (triangular truncation at wave number 62) in the MRF model. (1) gives 0.48K at 25 km horizontal grid spacing which is the grid spacing used in the present study. The choice of the values in (1), θ'_{max}, a, and Δx_0 are preliminary in this case study. Rogers and Fritsch(1996) selected optimal values of these parameters from sensitivity experiments for a single case. In this study, these values are presumably set to be applicable in a wide range of model grid sizes of 20 to 300 km. However, they can be calibrabrated by testing this trigger on a daily basis in numerical weather prediction models and applying it to climate modeling. These cautionary remarks also apply to the constants, c_1 and c_2 in (4), and c_3 in (5).

For the turbulence induced buoyancy contribution, the scaled virtual temperature excess near the surface, derived from the turbulence parameterization of the boundary-layer model (Hong and Pan 1996) is introduced,

$$\theta'_{cbl} = b\frac{\overline{(w'\theta'_v)_0}}{w_s} = \gamma_T + \varepsilon\theta_a\gamma_q\,, \qquad (2)$$

where b is the nondimensional constant which depends on the surface layer similarity relationship. Following the derivation of Hong and Pan(1996), the profile function of surface layer physics in the RSM leads to b=7.8. $\overline{(w'\theta'_v)_0}$ is the virtual heat flux at the surface layer, which is a function of temperature and moisture flux terms. w_s is the vertical velocity scale(=$u_*\phi_m^{-1}$, where u_* is the

surface frictional velocity scale, and ϕ_m is the wind profile function evaluated at the top of the surface layer.)(see Hong and Pan (1996)* for the details). On the right hand side, θ_a represents the temperature at the lowest model level, and ε the coefficient in the virtual temperature formula (=0.608). Note that the scaled temperature excess in (2) contains not only a temperature perturbation (=γ_T) but also a moisture term (=γ_q). A typical diurnal variation of γ_T and γ_q , PBL height, and wind speed at 10 m height above the surface is presented in Fig. 1. The γ_T evolves typically in proportion to the surface heat flux, and ranges from a maximum of 1-2 K during the daytime to nearly zero at night. The γ_q has less diurnal variation than the temperature contribution since surface moisture is not so strongly related to solar heating. We have noticed, however, that the γ_q can be unrealistically large when surface wind is very small. This large γ_q does not harm the turbulence diffusion because the vertical diffusivity coefficient in that situation becomes very small (refer p.2324 in Hong and Pan (1996) for a more discussion). Unfortunately, this large value is not reasonable in estimating moisture perturbation for this study. Thus, the total perturbation in (2) is constrained to be between 0 and 2K. The PBL height (Fig. 1b) has a diurnal cycle with maximum at early afternoon. Note that the PBL height remains high even when surface flux dies out. This is because the PBL height is calculated by the bulk Richardson number with a minimum of 0.5 between the surface layer and a certain model level. In Fig. 1c, it can be seen that the PBL height increases in the presence of strong winds after sunset. This is due to dynamical mixing. As described in Hong and Pan(1996), the turbulence parameterization in the RSM is strongly coupled to the surface energy budget, and in turn the new convection package is explicitly coupled to boundary layer and surface layer physics formulations.

*Note that (4) and (9) of Hong and Pan(1996) need to be corrected. The PBL height, h, should be in the denominator in (4), while it should be taken out in (9) of their paper.

The maximum temperature perturbation arising from subgrid scale inhomogeneities and from subgrid scale convective boundary layer forcing can be expressed by,

$$\theta'_{buoy} = \theta'_{sfc} + \theta'_{cbl} \quad , \tag{3}$$

and is decreased for regions where the source layer is above the PBL,

$$\theta'_p = \theta'_{buoy} \exp - \left(c_1 (\Delta z_{SL})^2 + \frac{c_2 \partial \theta_v}{\overline{\theta_v} \partial z} \right) \tag{4}$$

where Δz_{sl} is the distance between the top of the boundary layer and the mid-height of the source layer(h_{sl}), $\overline{\theta_v}$ is the mean virtual potential temperature(K) between the boundary layer top and the source layer , $\frac{\partial \theta_v}{\partial z}$ is the stability within Δz_{sl}, and c_1 and c_2 are constants set to $5 \times 10^{-7} \mathrm{m}^{-2}$ and 3×10^4 m, respectively.

In contrast to Rogers and Fritsch(1996), the decrease of perturbation with the distance of source layer from the surface is not considered in (1). However, this effect is taken into account in (4) as the buoyancy contribution term. We assume that the subgrid scale forcing due to surface

inhomogeneities is a constant below the PBL and decreases exponentially when the source is located above the PBL. As explained above, a PBL height can be above a surface layer even when surface heating is stopped (Fig. 1). Therefore, during the nighttime, dynamically induced turbulence forcing determines the subgrid scale buoyancy contribution. As a final step, the impact of large scale motion is also considered, as in Rogers and Fritsch(1996), where the buoyancy is increased (decreased) depending upon convergence(divergence) in the source layer, and is given by

$$\theta' = \theta'_p\left(1+c_3\Delta x\left(\frac{\partial \overline{w}}{\partial p}\right)^{1/3}\right), \tag{5}$$

where $\overline{w}$ is the grid scale pressure vertical velocity, and c_3 is a constant of 3×10^{-4} $m^{-1}s^{1/3}$. Δx in (5) accounts for the grid size dependency of $\overline{w}$, while this consideration is not taken into account in Rogers and Fritsch(1996). The qualitative basis for (5) is Chen and Orville's (1980) study of numerically simulated clouds that develop in low-level convergent fields. Their results show that bigger, deeper clouds develop in the presence of low-level convergence than when there is little or no convergence.

As in the operational trigger, the level of maximum moist static energy for the layer between the surface and 400 hPa above the surface is used for an updraft-air originating level. The buoyancy of a parcel is checked by comparing the moist static energy of the parcel with that of the environment at the LCL, which is the cloud base. The cloud top is determined by searching the first negative buoyancy level from the cloud base upward. The virtual temperature perturbation

calculated from (1)-(5) is taken into account in checking the parcel buoyancy at the cloud base and in determining the cloud top. This consideration enables the parcel be less inhibited by the capping inversion that restrains convection when the initial convection appears in a conditionally unstable atmosphere. In order to satisfy the enthalpy conservation within a cloud, the cloud work function is computed on the cloud property without the perturbation. In other words, the virtual temperature perturbation affects only the trigger in the convective parameterization scheme. *Note that the operational and new triggers differ not only in the buoyancy checking of the updraft parcel, but also, in the cloud base determination, which is the LFC for the former one, and the LCL for the latter one.*

In this study, it is assumed that the thermal will be buoyant at the cloud base if its temperature is greater than that of environment. On the other hand, one may argue that the buoyant energy between the source level and the cloud base has to be considered. This is not taken into account in this study because the parcel would be likely to have a minimum buoyancy at a LCL. This is based on the observational characteristics of convective systems discussed in Zhang and McFarlane (1991). They investigated the convective stabilization effect on the large-scale atmosphere by the composite analysis of upper-air sounding data sets obtained from PRE-STORM, and found that negative buoyancy appears below 720 hPa with its minimum near the LCL. One may also argue that the integrated buoyancy would be important, rather than the buoyancy at the LCL. For example, a small temperature deficit over a deep layer may be more effective at suppressing convection than a very stable, but shallow layer. This point is not taken into account here. However, it is most likely that a temperature deficit does not often exist since the enhanced parcel temperature is used to check the buoyancy of a parcel. Furthermore, subsequent checking

determines whether a cloud has enough buoyancy to initiate convection, as described in section 2c.

4. Case description and experimental design

a. Case description

In Figs. 2 and 3, we show the surface and 500 hPa analyses at 1200 UTC 15, 16 and 17 May 1995, respectively. The surface maps are extracted from the daily weather maps issued by the NCEP. The 500 hPa maps are constructed from the operational Global Data Assimilation System (GDAS) (Kanamitsu 1989) product. At 1200 UTC 15 May 1995 (Figs. 2a, 3a) (model initialization time) a stationary front extended from Texas to the Virginia-North Carolina border. To the north of this front, a high pressure system was centered at the border between Kansas and Missouri. At 500 hPa, a cutoff low appeared to be nearly equivalent barotropic over the west coast; little temperature advection was evident in any quadrant. There was no precipitation in Great Plains at this time. By 1200 UTC 16 May 1995(Figs. 2b, 3b), a low pressure system in mid-western Canada had crossed the US-Canada border with its center in Minnesota. As a result, a long frontal line extending from Minnesota southwestward to New Mexico had developed. Meanwhile, a surface front that was located over the south-central Unites States at 1200 UTC 15 had moved northeastward through Missouri and a frontal circulation had formed in the Great Plains. At 500 hPa, the cutoff low remained stationary and a weakening of its intensity was indicated by an increase of geopotential height at the low center. Ahead of this cutoff low a thermal ridge extended from Texas to Wisconsin. To the east of this thermal ridge, weak southwesterly flow advecting warm air to Kansas and Missouri is visible. More apparent is the

warm advection at 700 hPa(Fig. 4) in northern Texas, Oklahoma, Arkansas, Kansas, and Missouri. At this level, northwesterly flow behind the pressure trough from North Dakota to Iowa advected cold air southward. These simultaneous increases in the cold and warm advection are indicative of baroclinic energy conversion for surface cyclogenesis. During the 24hour period between 1200 UTC 15 and 1200 UTC 16 May 1995, rainfall was observed in northern Texas, along with an east-west oriented area over Kansas, Missouri, and Illinois (Fig. 5a). At 1200UTC 17 (Fig. 2c), as the surface low pressure system centered in Minnesota moved northeastward, a cold front surged southeastward extending from Texas to the Great Lakes region. A continental high pressure system with dry and cold air can be found to the north of this front. At 500 hPa (Fig. 3c), as the cutoff low moved eastward to the Colorado-New Mexico border, the system became more baroclinic as the southwesterly wind intensified to the east of this low, and cold advection behind the pressure trough became better organized. Significant precipitation was found ahead of the cold front (Fig. 5b). A large area of 24-h accumulated rain greater than 32 mm covered Kansas, Missouri and Illinois. To the west of this heavy rainfall was an area of lighter precipitation over southeastern Wyoming, western Nebraska, and eastern Colorado. This rainfall seemed to be associated with upslope flow along the eastern Rockies embedded in the north-south oriented surface front.

The rainfall in Kansas, Missouri and Illinois was located in the same area for two consecutive days. This persistent rainfall led to flooding in this region. Reflecting the absence of baroclinicity at 500 hPa by 1200 UTC 16 May 1995, rainfall in that region seems to be associated with the surface warm front propagating northeastward from 1200 UTC 15 to 1200 UTC 16 May 1995 (Figs. 2a and b). It is most likely that the precipitation in the Great Plains during this period

is not directly associated with baroclinic processes in the upper troposphere but is formed by frontal cyclogenesis confined in the lower tropospheric level. The upper air analyses (not shown) revealed the barotropic structure associated with the cut-off low in southern California continued until 1200 UTC 16 May 1995. After 1200 UTC 16 May 1995, precipitation in Kansas, Missouri, and Illinois formed ahead of the cold front advancing southeastward. This cold front intensified as the cut-off low finally moved eastward. Thus, rainfall during this second 24h period seemed to be highly associated with baroclinic processes in the upper troposphere. The frontal system slowly traveled eastward after 1200 UTC 17 May 1995 with heavy rainfall accompanying it in eastern United Sates, centered in Illinois and Indiana regions.

b. Experimental design

In this study, we used the RSM which has the physics of the MRF model as of June 1996. The RSM has a nominal horizontal resolution of 25 km over the United States and a vertical resolution of 28 layers in the sigma coordinate system. Fig. 6 shows the model integration domain with the model orography. Because of the computer resources, the domain is not big enough to avoid a possible lateral boundary problem. However, it is large enough to focus on the precipitation forecast over the Great Plains. With this resolution, orography is resolved in some detail. For example, a sharp gradient of orography over the California coastal region in an east-west direction is distinct. Mountains over California and Colorado are higher than 3000 m. On the other hand, the negative values over ocean come from the spectral representation of the orography. The lowest model level has a sigma value of 0.995 which corresponds to about 30-50 m above the surface. The pressure at the model top layer for prognostic variables is about 5 hPa. Initial data are interpolated from the operational GDAS. Base fields and boundary conditions are

updated from the 6 hourly MRF model output which has a resolution of T126 (triangular truncation at wave number 126). The model is integrated for 48 hours starting from 1200 UTC 15 May 1995.

Table 1. Summary of numerical experiments

No.	Code	Convective trigger function	Grid scale precipitation scheme	Domain averaged total (grid-resolvable) rain, mm/48 hours	Precipitation skill score (ETS)
	OBS			2.82	
1	OP1M	Operational trigger	Diagnostic liquid species	6.69 (4.59)	0.119
2	TR1M	New trigger	Diagnostic liquid species	6.94 (4.14)	0.125
3	OP3M	Operational trigger	Prognostic liquid species	6.00 (2.79)	0.101
4	TR3M	New trigger	Prognostic liquid species	6.00 (2.52)	0.183
5	NOPT	New trigger with $\theta'=0$ in (5)	Prognostic liquid species	5.94 (2.72)	0.177

As summarized in Table 1, five experiments were designed to permit investigation of the impact of the convective trigger formalism. In the table, the operational trigger in the convection scheme includes the formalism described in section 2c, while the new convective trigger includes the modifications discussed in section 3. The #M represents the number of water substance categories in the grid-resolvable physics. The OP1M experiment employs the current operational precipitation physics in the MRF model which were described in section 2. The TR1M experiment which employs the new trigger, is to investigate the impact of triggering function within the simple

diagnostic grid-resolvable precipitation physics. The comparison of the OP3M and TR3M experiments are the same to that of the OP1M and TR1M experiments, except for a more sophisticated grid-resolvable precipitation process.

The prognostic liquid phase scheme used in this study has three prognostic variables for water substance, including one for water vapor and 2 for hydrometers with ice microphysical processes as developed by Dudhia (1989). Implementation and intercomparison of various cloud schemes are given in Hong et al. (1998). The NOPT experiment is identical with the TR3M experiment, but removes the subgrid scale buoyancy contribution in (5). This experiment demonstrates the importance of the subgrid scale perturbation in the new trigger formalism.

Also shown in Table 1 is the 48-h accumulated domain averaged rain. The value in the parenthesis represents the grid-resolvable rain contribution to the total rain. The equivalent threat scores(ETS) of the precipitation forecast are presented to compare the skill of precipitation forecasts. Whereas the simple threat score is the quotient of the intersection of the observed and forecast areas of precipitation divided by the union of these areas, the ETS refines the definition by accounting for apparent skill derived only from random chance (Rogers et al. 1996). The scores are computed over the United States using forecast precipitation and observed precipitation computed by averaging rain gage data within each model grid cell. Scores are averaged in precipitation categories for the two day forecast period. Together with domain averaged total precipitation amount, the ETS gives a measure of the skill of precipitation forecasts. Values in the table are the average over all precipitation categories. Although the ETS in each precipitation category is robust in representing the precipitation skill, the average seems to be sufficient to compare the skill of precipitation predictions from each experiment for a single case study. It is

important to note that at NCEP the ETS and bias scores are routinely computed at 80 km grid. Both model forecasts and observations are interpolated to that grid. Hence, higher precipitation biases from the model are not only due to the model's error but also due to the lack of observations every 25 km over United States. This results in the reduction of the ETS when it is computed on 80 km grid. Therefore, comparison of the scores in Table 1 is valuable, but not for its absolute magnitude. From the table, it is evident that the TR3M experiment had the best performance.

5. Results and discussion

a. Synoptic pattern

As mentioned earlier, the TR3M experiment produced the best results in terms of precipitation forecast. In Fig. 7, the 500 hPa geopotential height, temperature distribution, and wind vectors at 1200 UTC 16 and 1200 UTC 17 from the TR3M experiment are presented. Overall, the model predicted the synoptic patterns associated with the heavy precipitation event rather well. For example, the model correctly forecastes the position and intensity of the cut-off low during the two day period. The low stayed over California for the 24-h forecast period valid at 1200 UTC 16 and then traveled eastward as heavy precipitation occurred over Kansas. In addition, the southward progress of a trough, initially centered over central Canada, was very we simulated. In association with precipitation over Kansas and Missouri during the forecast time, th model reproduced the intensification of a thermal ridge over Kansas and Missouri at 1200 UTC At 48-h (1200 UTC 17)(Fig. 7b), the thermal ridge, ahead of a cutoff low, was also well simulated.

The other experiments also reproduced large scale patterns that compare well to those from the TR3M experiment. They include the movement of the cut-off low, the intensification of baroclinicity, and the development of thermal ridge ahead of a pressure trough. However, differences between the experiments with the operational and new triggers were distinct where heavy precipitation was simulated. The impact of different grid-resolvable physics on the large scale pattern was described in Hong et al.(1998). From Fig. 8, it can be seen that compared to the results from the TR3M experiment a cold bias was dominant over the heavy precipitation region in the lower troposphere in the OP3M experiment. The thermal ridge ahead of the pressure trough was weaker in the experiments with the operational trigger. In the 48-h forecast, this colder area extended eastward toward the eastern United States. In the middle to upper troposphere, the difference field shows a less distinct cold bais acompanied by a highly complicated pattern because of the nonlinear feedback between the precipitation physics with the larger-scale patterns.

b. Precipitation forecast skill

In Fig. 9, we show the predicted 24-h accumulated precipitation valid at 1200 UTC 16, and 1200 UTC 17 May 1995 resulting from the OP1M and TR1M experiments. In the 24-h forecast using the operational physics (Fig. 9a), the model produced excessive rainfall over Kansas and northwestern Texas, which is due to grid-resolvable precipitation physics(dotted lines in the figures). The maximum amount of grid-resolvable precipitation over Kansas is as high as 200 mm.

In the 48-h forecast (Fig. 9b), the major precipitation area extended eastward from Missouri through West Virginia, which is too far to the east (cf. Figs. 5 and 9). The model also overestimated the rainfall over Colorado, Oklahoma, and southern Michigan and Wisconsin, which is mostly due to grid-resolvable precipitation physics. The maximum amount of grid-resolvable rain

in that region is as high as 100 mm. In contrast to the excessive rainfall due to grid-scale rain, the subgrid scale rain is relatively weak and widespread. A small area of 24-h accumulated rain greater than 32 mm appears in Missouri. The area greater than 16 mm enclosing the 32 mm contour is oriented northeastward from central Missouri to central Illinois.

Compared to the results from the OP1M experiment, the TR1M experiment enhances the precipitation forecast skill; the ETS increased from 0.119 to 0.125. The total amount of precipitation during the 48-hr forecast period also increased (Table 1). The reason why the total precipitation is enhanced is unclear. However, it is worth noting that in the 24-h forecast period ending at 1200 UTC 16, grid-resolvable rain is significantly reduced (Fig. 9c). The updated convective trigger removes the excessive rainfall due to grid-resolvable precipitation physics in Kansas, and northwestern Texas. In the 48-hr forecast period (Fig. 9d), the major grid-resolvable precipitation area extended eastward from Missouri to Virginia and has the axis notably to the south, while this axis is too far to the northeast in the OP1M experiment (Fig. 9b).

In Fig. 10, the comparison of the 24-h accumulated precipitation from the OP3M, TR3M, and NOPT experiments is shown. Overall, it can be seen that for grid-scale precipitation, the impact of the operational and new triggers with the sophisticated microphysical processes on the precipitation distribution is comparable to when the diagnostic cloud is employed. For example, the OP3M experiment with the operational trigger produces widespread light subgrid scale rain compared with that from the TR3M experiment. In the 24-h forecast, the model with the operational trigger still shows the excessive grid-resolvable rain over Kansas, and to the southeast of this grid-resolvable rain area subgrid scale rain appears which is too widespread. The excessive grid-resolvable rain over northwestern Texas is not reduced. The degradation of precipitation skill

is more prominent in the 48-h forecast (compare Figs. 10b and 10d). The subgrid scale rain area from the OP3M experiment is centered over Missouri and southern Illinois, which is not far from what the new trigger shows. However, the subgrid scale rain is widespread compared to what the new trigger produced. As a result, the operational trigger tends to separate the grid-resolvable rai and subgrid scale rain over the heavy precipitation area, which leads to significant degradation of the precipitation forecast skill. The ETSs from the OP3M and TR3M runs are 0.101 to 0.183, respectively(Table 1). The degradation of the scores by the OP3M experiment was found to be caused by underestimating heavy precipitation amounts and overpredicting the area of light rainfall. The precipitation forecast skill from the OP3M run is even worse than that from the OP1M experiment with the diagnostic cloud scheme for grid-resolvable precipitation physics. The ETSs from the OP3M and OP1M runs are 0.119 and 1.101, respectively. This implies that sophisticated microphysical processes alone do not guarantees the improvement of forecast skill. The comparison of different microphysical processes on the predicted precipitation are discussed in Hong et al. (1998).

From Figs. 10e and f (NOPT experiment), it can be seen that the impact of the temperature perturbation in (5) on the predicted precipitation, while not negligible, is not significant enough to account for the difference in the distribution of precipitation between the OP3M and TR3M experiments. Overall, the NOPT experiment produces less subgrid scale rain and more grid-resolvable rain than the TR3M experiment (Table 1, Fig. 11). As in the case of the comparison of two different triggers, a more significant difference is found in the distribution of grid-resolvable precipitation. For example, a more concentrated grid-resolvable rain is predicted by the NOPT experiment on the border between Kansas and Missouri for the 24-h forecast. In the 48-h forecast,

the area of grid-resolvable rain from the NOPT experiment is much larger than the TR3M experiment. The impact of the perturbation buoyancy is further discussed in section 5d.

An important result shown in this section is that the grid-resolvable rain from Indiana eastward valid at 1200 UTC 17 May 1995 is more influenced by the convective parameterization than by the change in the grid-resolvable algorithm. (Compare Figs. 9b and 9d, and 10b, 10d). This outcome follows the arguments of Kuo et al.(1996), obtained in a systematic evaluation of precipitation physics in the simulation of marine cyclogenesis. In that research it was determined that the distribution and intensity of precipitation, and its partitioning into grid-resolvable and subgrid scale portions, were extremely sensitive to the choice of convective parameterization scheme.

c. Comparison of the two convective trigger functions

As discussed in the previous section, for grid-scale precipitation, the impact of the operational and new triggers with the sophisticated microphysical processes on the precipitation distribution is comparable to when the diagnostic cloud scheme is employed. Therefore, more attention will be paid to the comparison of the OP3M and TR3M experiments.

Note that the two triggers differ not only in inclusion of perturbation buoyancy, but also in bouancy checking of the updraft parcel and cloud base determination. In the operational trigger the depth between the updraft-air originating level and the LFC should be less than 150 hPa to initiate convection, while the new trigger checks the parcel's buoyancy at the LCL. The cloud base for the operational and new triggers is determined as the LFC and LCL, respectively. Note also

that the entrainment of an updraft parcel and the detrainment of a downdraft parcel in the convection scheme are confined between the updraft originating level and the cloud base and the amounts of mixing of a parcel with that in the environment are propotional to the depth between the two levels.

Since the interaction between subgrid scale and grid-resolvable rain processes is intimately related and highly complicated in a three-dimensional model frame work, a detailed illustration of the impact of convective trigger function on the predicted precipitation is focused on the 24-h forecast when the subgrid scale rain is dominant and before the grid-resolvable rain is initiated. Comparisons of the results from the OP3M and TR3M experiments are given for three grid points, marked in Fig. 10a. One grid point is located in Missouri (point A, near Springfield, Missouri), and two grid points in Kansas (point B, near Russell Kansas and point C, near Wichita, Kansas). A summary of precipitation amount during the first 24-h forecast period at those grid points is given in Table 2. The point A represents the area over which the OP3M experiment with the operational trigger produced rain during the first 24-h forecast period, while the TR3M experiment with the new trigger produced very little rain. The points B and C represent the areas where the OP3M experiment produced the subgrid scale and grid scale rain together, while only subgrid scale rain appeared in the new trigger experiment. At the point B, the two experiments produced comparable amount of total rain, while the operational trigger produced excessive grid-scale rain at the point C.

Table 2. 24-h accumulated total (subgrid scale) precipitation amount (mm) from the TR3M and OP3M experiments, valid at 1200 UTC 16 May 1995 at the points, "A', "B", and "C", marked in Fig. 10a. Corresponding observed amount is also shown.

The grid point	Total (subgrid scale) precipitation amount (mm)		
	OP3M	TR3M	OBS
"A"	21.0 (21.0)	0.7(0.7)	1.0
"B"	7.6 (1.4)	7.5(7.5)	3.0
"C"	23.9 (7.5)	7.7(7.7)	4.0

Figure 12 shows the temporal evolution of hourly rainfall from the OP3M experiment, together with the equivalent potential temperature (θ_e) and saturated equivalent potential temperature (θ_{es}) profiles at point A (marked in Fig. 10a) in the presence of convective initiation. There was no grid-scale precipitation. From the profile, the parcel originating level is 940 hPa and the LFC is 800 hPa. The depth between the two levels satisfies the convection initiation by the operational trigger. However, the new trigger does not initiate convection because the parcel originating at 940 hPa has a negative buoyancy at the LCL, which is 875 hPa. This kind of thermodynamic profile is not unusual during the nighttime when surface layer cools. It can be deduced that the operational trigger tends to initiate convection more often than the new trigger, even when subcloud layer is dry. This is because the operational trigger does not check humidity of the environment. It is clear from the evolution of domain averaged precipitation amounts, as shown

in Fig. 12, that the operational trigger yields more convection during the nighttime than the new trigger.

In Fig. 13, we compare the temporal evolution of the rainfall and vertical distribution of relative humidity at the point B (marked in Fig. 10a). The rain in the TR3M experiment starts at 0548 UTC and lasts about 4 hours with a short break at 0630 UTC. On the other hand, subgrid scale rain started at 0224 UTC in the OP3M experiment with the operational trigger which is about 3 hours earlier than in the TR3M experiment. Also in the TR3M experiment, several time steps later, grid-resolvable rain is initiated and lasts about 4 hours with a higher intensity than subgrid scale rain. Differences in large-scale environments by both schemes can be visualized from the evolution of relative humidity (Figs. 13c and 13d). As convection is initiated, the OP3M experiment shows the increase of relative humidity within the entire troposphere. Over time, a saturated layer in the upper level extends down to middle troposphere below 600 hPa. In the TR3M experiment, the increase in relative humidity appears centered at the parcel originating level, 875 hPa prior to convective initiation. The saturation layer is limited to a shallow layer between 875-835 hPa, and relative humidity decreases as convection decays.

The reason for the different partitioning of subgrid and grid resolvable scale rain can be explained by a comparison of the thermodynamic profiles, as shown in Fig. 14. From the figure it can be seen that the new trigger initiates convection when CAPE is large enough and the source level, which is 875 hPa, is nearly saturated. It is due to the fact that the new trigger checks the buoyancy of the parcel at the LCL while the operational trigger checks the depth between the source level and LFC. As a result, the new trigger initiates convection when the subcloud layer is moister while the operational trigger develops the convection even when the subcloud layer is dry.

In addition to the timing of convective initiation, another factor exists to cause for the operational trigger to removes less CAPE. Note that the convection scheme reduces the buoyancy of the updraft parcel by entrainment. Because of a larger entrainment of the updraft parcel due to a longer distance between the cloud base and the updraft-air originating level, the operational trigger tends to remove less CAPE than the new trigger. Initiating convection in such a weak CAPE condition adds water vapor to nearly saturated middle to upper troposphere by detraining process at the cloud top. From the analyses of $q_{ci}$and q_{rs} (not shown), it was found that in the operational trigger experiment, the falling snow from pre-existing ice crystals grows at the expense of this water vapor in the middle atmosphere and forms grid-scale rain, while in the TR3M experiment the falling snow in the middle atmosphere is removed by sublimation process because water vapor is detrained in the higher troposphere. Although the total rainfall amount at point B is comparable for both experiments, the resulting synoptic patterns due to different heating characteristics can be very different. This issue will be further discussed at the end of this section.

In Fig. 15, we compare the temporal evolution of the rainfall and vertical distribution of relative humidity at the point C(marked in Fig. 10a). Precipitation in the TR3M experiment with the new trigger appears at 0400 UTC and lasts about 3 hours. On the other hand, the OP3M experiment with the operational trigger produces subgrid scale rain starting at 0300 UTC which is about 1 hour earlier than the TR3M experiment. At 0430 UTC, major grid-resolvable rain starts and lasts about 2 hours with a higher intensity than the subgrid scale rain. From the comparison of relative humidity(Figs. 15 c and d), both experiments show a saturated layer at about 875 hPa level as the convection is initiated. A primary difference between two experiments is that the operational trigger develops a deep saturated layer centered at 875 hPa and eventually extends to

the entire troposphere after 0500 UTC. However, as in the case of the point B, the saturation from the TR3M experiment is limited to a shallow layer between 875-835 hPa, and relative humidity decreases as convection decays.

To illustrate the contrast in the initiation of convection by each trigger, θ_e and θ_{es} are compared at the point C as shown in Fig. 16. The profiles were constructed just before the onset of convection and one hour later for each experiment. Note that the difference in timing of onset at this grid point is less than an hour, while at point B the operational trigger initiates convection about 3 hours earlier than the new trigger. Therefore, subcloud layer for both experiments is very similar with a nearly saturated layer prior to initiating convection. Both experiments also have the same parcel originating level, which is the maximum θ_e level at 875 hPa. Despite these agreements, the adjusted temperature and moisture profiles diverge accompanied by excessive rainfall from the operational trigger experiment (Table 2). The primary reason for this difference is in cloud base determination. The new trigger checks the buoyancy of the parcel at the LCL while the operational trigger checks the depth between the source level and LFC. In the TR3M experiment the parcel at the source level is nearly saturated, so that the cloud base, the LCL, is 835 hPa. In the OP3M experiment with the operational trigger, the cloud base is the LFC determined as the first positive buoyancy level by conserving θ_e at the source level, which is 735 hPa. Consequently, the primarily difference between the two triggers is the depth between the source level and the cloud base. The depth is 35 hPa and 140 hPa for the TR3M and OP3M experiments, respectively. As explained in the case of the point B, the operational trigger results in less buoyancy of the updraft air parcel than the new trigger due to more entrainment over a deeper subcloud layer, thus a less removal of CAPE.

Realizing the fact that the detrainment of the downdraft parcel is limited to the layer between the cloud base and the updraft-air originating level and results in moistening and cooling the environmental air, the experiment with the operational trigger has more chance to become saturated. Consequently, in the OP3M experiment, the LFC becomes close to the LCL as convection continues, eventually producing an absolutely unstable layer between the LFC and the updraft-air originating level. This absolutely unstable layer experiences upward motion due to grid resolved forcing. Conditions are such that cumulus parameterization initiates in the TR3M experiment with the new trigger because of less mixing of updraft and downdraft air. However, in the OP3M experiment relative humidity simply keeps rising until saturation is reached above the cloud base. The existence of saturation in a conditionally and convectively unstable sounding abov the LCL produces an unrealistic situation. In particular, because the resolvable-scale heating maximum occurs at relatively lower levels in the OP3M experiment, it tends to enhance the lower-level moisture convergence more efficiently than those with a higher-level heating maximum in the TR3M experiment. Eventually a deep dry-adiabatic but saturated layer forms as the heating layer deepens. This layer rapidly overturns, producing intense precipitation on the grid scale.

Despite the impacts of two trigger functions at three grid points described above, one may speculate the importance of the specification of cloud base. To confirm this, two preliminary experiments (not shown) were conducted, one is the new trigger with the cloud base at the LFC, and the other is the operational trigger with the cloud base at the LCL. In the 24-h forecast valid at 1200 UTC 16, the former experiment showed the heavy precipitation confined in Kansas as in the TR3M experiment, but with much of grid-scale rain as in the OP3M experiment. In the 48-h forecast, the distribution of precipitation was very comparable to that from the OP3M experimen

The latter experiment with the operational trigger with the cloud base at the LCL showed a very similar distribution of precipitation to that in the OP3M run during the first 24 forecast. In the 48-h forecast, the distribution of precipitation was between the OP3M and TR3M experiments. These experiments suggest that the parameter to which two different trigger experiments are most sensitive is the buoyancy checking of the updraft parcel. As shown in the point C, the specification of cloud base mainly affects the cloud properties such as the entrainment of updraft and the detrainment of downdraft, and following partition of subgrid and grid scale rain, so that its impact is large after the 24-h forecast, when heavy precipitation is simulated.

On the other hand, the unrealistically generated excessive rain at a grid point from the operational trigger experiment was pointed out by Molinari and Dudeck(1986) and Zhang et al.(1988). They found that either grid-scale precipitation physics alone or combination of parameterized convection and diagnostic explicit cloud scheme for grid-resolvable precipitation physics induces a runaway type of positive feedback among latent heat release, larger-scale moisture convergence and the surface pressure fall. By contrast, the same scenario was found in this study by introducing a subtle change in the convective trigger, even though the cumulus parameterization scheme and prognostic cloud scheme incorporating water loading and melting are separately responsible for subgrid scale and grid-resolvable precipitation physics. This excessive rainfall problem is more serious when diagnostic cloud is employed for grid-resolvable precipitation physics, as shown in Fig. 9. This is due to the lack of stabilizing microphysical processes such as evaporation, water loading and melting processes as shown in our companion paper (Hong et al. 1998), and pointed out earlier by Zhang et al. (1988). From these findings we can say that the realistic treatment of precipitation physics in a mesoscale model does not only

depend upon what kind of combination of physical processes is employed, but also how the interaction between the subgrid scale and grid resolvable precipitation physics is represented.

From Figs. 13c, 14a, 15c, and 16a, it can be seen that compared to the operational trigger the new trigger tends to initiate convection in the presence of a moist subcloud layer and to mix weakly the updraft parcel with the environment, leading to a deeper cloud with a large cloud work function. This characteristic is in line with the initiation of deep moist convection found by Ziegler et al.(1997), which is the combination of deep mesoscale lift, weak mixing following the motion, and high boundary layer humidities appears to be necessary for deep convection to form near the dryline. Another interesting feature in the TR3M experiment with the new trigger is the generation of saturated layer in the subcloud layer. These unstably stratified saturated layers around the cloud base are in line with the recent finding from the modeling study for convection at the dryline (Ziegler et al. 1997). The explicit treatment of mircophysical processes without parameterized convection was utilized in a 5 km grid mesh for their study. According to their results, the absolutely, convectively unstable stratification of the saturated layers were found in the active stage of deep convection at the dry line, and were explained as a transient state that arises from the strong mesoscale lifting of air parcels with warm and moist air. This saturated layer was also found from an analytical modeling study in a cloud model by Crook and Moncrieff(1988). They investigated the effect of large-scale convergence on the generation and maintenance of deep moist convection, and speculated that this saturated layer formed just prior to convection in the presence of large-scale convergence.

Note that the total amount of rain is nearly the same during the 48-h forecast period (Table 1) for both runs. This implies that despite the significant differences in the distribution and intensity

of subgrid scale rain and grid-resolvable rain, the total amount of water vapor processed is about the same for both the OP3M and TR3M experiments. This coincidence does not seem to be valid all the time because the heavy precipitation in this case lasts after the integration period. Despite this coincidence, the resulting feedback to large scale is quite different, as explained in the comparison of thermodynamic profiles. The new trigger redistributes the heat and moisture following the parameterized cloud evolution such as moistening and cooling in the subcloud layer due to downdrafts and drying and heating in the middle cloud layer and moistening and heating in the high cloud layer. On the other hand, in the OP3M experiment the heat and moisture distribution are mainly controlled by the grid-resolvable rain process, which follows the microphysical processes in the cloud scheme. The diabatic heating profiles for both experiments are not available. However, from the difference in synoptic scale feedback due to the different heating and moistening characteristics in the parameterized convection and grid-resolvable precipitation physics (Fig. 17), it can be deduced that the operational trigger experiment produces a more stabilized and moister environmental air than the new trigger experiment. Because of these differences that occur by the 24-h forecast time, the forecasts diverged thereafter. These changes in the larger-scale patterns downstream in the 48-h forecast due to changes in the convective forcing in the 24-h forecast was also pointed out by Zhang and Harvey(1995). Note that the OP1M and OP3M experiments with the operational trigger have very similar axes for the grid-resolvable rain from Indiana eastward in the 48-h forecast, and that the TR1M and TR3M experiments with the new trigger have the axis notably to the south(Figs. 9 and 10). The importance of the subgrid scale thermal excess in (5) can be explained from the same point of view, comparing the TR3M and

NOPT experiments (Figs. 10d and 10f), even though the impact is smaller than that from the different convection triggers.

d. Impact of the temperature perturbation in the new convection trigger

As mentioned in section 5b, the impact of the temperature perturbation in the new convection trigger is not significant as to account for the difference in the two trigger experiments, but may be important to the successive development of precipitation system. It can be seen that the NOPT experiment produces less rain in northwestern Texas, southern Arkansas, northern Mississippi, and northern Alabama (Compare Figs. 10c and 10e). These areas are where the modeled convection was initiated in the afternoon (not shown). We compared the resulting rain from the TR3M and NOPT experiments at many points in those areas. In general, the TR3M experiment tended to generate convection earlier by a few hours than the NOPT experiment, implying that the subgrid scale buoyancy played a role in accelerating the initiation of convection by adding the perturbation to the parcel at the source level. Since the perturbation amount is high during the daytime due to boundary layer turbulence forcing (Fig. 1), the domain average of subgrid scale rain from the TR3M experiment is larger during the daytime than in the OP3M experiment (Fig. 11). Meanwhile, the relatively small impact of the buoyancy perturbation in the new trigger seems to be due to the fact that the convective precipitation in the model is initiated during the nighttime. However, it is likely that the subgrid scale buoyancy perturbation may be important when convection is initiated in the afternoon. It is also noted that the constants in Eqs. (1), (4), and (5) are preliminary, as discussed in section 3, from the perspective of operational implementation. More tests are being conducted to examine the precipitation distribution over the ocean for climate modeling as well as over land for daily weather forecasts.

6. Summary and concluding remarks

In this paper, a convective trigger function that explicitly couples the boundary layer turbulence and precipitating convection processes is proposed. The scheme is based on the Rogers and Fritsch (1996) concept that the subgrid scale perturbation is a combination of forcing due to surface inhomogeneities, boundary layer turbulence, and free atmospheric turbulence, and its modulation by grid scale vertical motion. The concept is adapted in this study in a modification of the simplified Arakawa-Schubert scheme (Grell 1993; Pan and Wu 1994; Hong and Pan 1996) used in the NCEP RSM. A major difference between the Rogers and Fritsch (1996) scheme and that used in this study is that a parcel method considering subgrid scale thermal buoyancy derived from the counter gradient mixing term of large eddy induced turbulent boundary layer (Hong and Pan 1996) is used instead of vertical velocity perturbation employed by Rogers and Fritsch. The scheme was implemented as a part of the new precipitation physics package for the NCEP RSM, together with a prognostic cloud scheme to improve the precipitation prediction skill during the convection season over United States. The package has been tested with a grid spacing of approximately 25 km over United States for a heavy rainfall case during 15-17 May 1995.

It is evident that the new convective trigger is capable of enhancing the precipitation predictability. The new trigger removes excessive rainfall due to grid-resolvable precipitation physics in Kansas, and northwestern Texas during the first 24-h forecast period. In the 48-h forecast period, the major grid-resolvable precipitation area in the forecast extended eastward from Missouri to Virginia, while this axis is too far to the northeast in the experiments with the operational trigger. The impact of the trigger change on the predicted precipitation is comparable

to that for grid-resolvable physics, either a simple diagnostic cloud scheme or a prognostic cloud scheme with sophisticated microphysics is employed.

Three major factors in the trigger mechanism are responsible for the difference in the precipitation forecast between the operational and new trigger experiments : 1) buoyancy checking of the updraft parcel; 2) cloud base determination; and 3) inclusion of perturbation buoyancy. Since the operational trigger tends to initiate convection even when subcloud layer is dry, it produces more convection during the nighttime than the new trigger. Because of a deeper mixing layer of the updraft parcel due to the difference in cloud base determination, the operational trigger activates with smaller values of CAPE. The above two reasons allow the operational trigger to initiate convection in situations with weaker CAPE than the new trigger. Initiating the convection in such conditions adds water vapor to nearly saturated middle to upper troposphere by the cloud top detrainment. This leads to the development of grid-scale rain at the expense of supersaturation, while the new trigger produces subgrid-scale rain. Although comparable amount of rainfall at the surface can exist in that situation, the feedback to larger scale is very different due to the different heating characteristics in the parameterized convection and grid-resolvable precipitation physics. On the other hand, the operational trigger tends to produce excessive grid-scale rain when convection is initiated in the presence of nearly saturated subcloud layers. This is not only because of the reduced buoyancy of the updraft parcel, but also because of the moistening and cooling of the environmental air due to the detrainment of the downdraft air. These findings reinforce previous studies(e.g., Zhang et al. 1994) in showing that *the realistic treatment of precipitation physics in a mesoscale model does not only depend upon what kind of combination of physical*

processes is employed, but also how the interaction between the subgrid scale and grid resolvable precipitation physics is represented.

Meanwhile, the new trigger tends to initiate convection in the presence of a moist subcloud layer and to mix weakly the updraft parcel with the environment, leading to a deep convection with a large cloud work function. This characteristic is in line with the profile of deep moist convection shown by Ziegler et al.(1997). Another interesting feature of the parameterized convection with the new trigger is the generation of a shallow saturated layer in the subcloud layer. The formation of this saturated dry adiabat can be explained by stabilizing the absolutely, convectively unstable layer due to the vertical diffusion processes. These existence of unstably stratified saturated layers around the cloud base is in line with the findings given by Ziegler et al.(1997) and Crook and Moncrieff (1988).

Another aspect of the results is that the location of the grid-resolvable rain is more influenced by the convective parameterization than by the change in the grid-resolvable precipitation algorithm. There is also a downstream impact of convective precipitation in the 24-h forecast so far to the distribution of grid-resolvable precipitation in the 48-h forecast. The significant impact of the grid-scale precipitation due to parameterized convection was addressed by Kuo et al.(1996). The significant changes in larger-scale patterns so far downstream due to changes in the convective forcing also was pointed out by Zhang and Harvey(1995). However, in this study the significant impacts are found to be due to a subtle change in parameterized convection, rather than either switching the parameterized convection scheme(Kuo et al. 1996) or removing the convective heating in the successive development of a cyclone(Zhang and Harvey 1995). This aspect of the experiments also warrants emphasis showing that the interaction

between convection and grid-resolvable precipitation physics is not just a local phenomenon, but rather a highly nonlinear feedback. Therefore, it is concluded that in a mesoscale model a proper treatment of subgrid scale precipitation (convection) physics is crucial to provide the favorable synoptic condition for grid-resolvable precipitation physics to be activated at the correct location and may be a prerequisite to realizing better precipitation physics.

The impact of the temperature perturbation in the new convection trigger is not so significant in this case study, but is not negligible for the successive development of precipitation system. The relatively small impact of the buoyancy perturbation in the new trigger seems to be due to the convective precipitation in the model being initiated during the nighttime. However, it is likely that the subgrid scale buoyancy perturbation may be important when convection is initiated in the afternoon. It is also noted that the constants in Eqs. (1), (4), and (5) are preliminary, as discussed in section 3, from the perspective of operational implementation. From a testing of the new convective trigger function in the MRF model with a resolution of T126, some improvement was found in the skill of the precipitation forecast over land, which accompanies a decrease in the lighter precipitation categories and an increase in the heavier precipitation categories. However, problems still remain in the convection over the ocean when model is integrated more than a month, which accompanies somewhat less precipitation over the western Pacific than what it should be. More tests are being conducted to improve the scheme by changing the parameters in estimating the subgrid-scale temperature perturbation.

Although the ETSs can provide an object measure of skill for precipitation forecasts, many uncertainties still remain in evaluating the performance of a mesoscale model. This is mainly because the routine ETSs at NCEP are calculated against the 24-h accumulated rain gauge data,

whose spatial distribution is much more sparse than the model grid spacing. A new hourly precipitation archive combining rain gauge data and radar estimates is under development for use at NCEP (Baldwin and Mitchell 1996) that may be more appropriate for the evaluation of mesoscale mdoel forecasts.

Acknowledgments

The authors would like to thank Jack Kain and two anonymous reviewers, whose comments and suggestions improved the clarity of the paper. The authors also would like to express their gratitude to Joseph Gerrity and Shrinivas Moorthi for generous internal reviews.

REFERENCES

Arakawa, A. and W. H. Shubert, 1974: Interaction of a cumulus ensemble with the large-scale environment, Part I. *J. Atmos. Sci.*, 31, 674-704.

Baldwin, M. E., and K. E. Mitchell, 1996 : The NCEP hourly multi-sensor U.S. precipitation analysis. 11th conference on numerical weather prediction, August 9-13, Norfolk, Virginia.

Chen, C., and H.D. Orville, 1980 : Effects of mesoscale convergence on cloud convection. *J. Appl. Meteor.,* 19, 256-274.

Crook, N. A., and M. W. Moncrieff, 1988 : The effects of large-scale convergence on the generation and maintenance of deep moist convection. *J. Atmos. Sci.*, 45, 3606-3624.

Dudhia, 1989: Numerical study of convection observed during the winter monsoon experiment using a mesoscale two-dimensional model. *J. Atmos. Sci.*, 46, 3077-3107.

Emanuel, K. A. and D. J. Raymond, 1992 : Report from a workshop on cumulus parameterization. *Bull. Amer. Meteor. Soc.*, 73, 318-325.

Grell, G. A., 1993 : Prognostic evaluation of assumptions used by cumulus parameterization. *Mon. Wea. Rev.,* 121, 764-787.

Hong S.-Y. and H.-L. Pan, 1996 : Nonlocal boundary layer vertical diffusion in a medium-range forecast model. *Mon. Wea. Rev.*, 124, 2322-2339.

_____, H.-M. H. Juang, and Q. Zhao, 1998 : Implementation of prognostic cloud scheme for a regional spectral model. *Mon. Wea. Rev.,*

Juang, H.-M. H. and M. Kanamitsu, 1994 : The NMC nested regional spectral model. *Mon. Wea. Rev.*, 122, 3-26.

_____, S.-Y. Hong, and M. Kanamitsu, 1997 : The NCEP regional spectral model: An update. *Bull. Amer. Meteor. Soc.*, 78, 2125-2143.

Kain, J. S. and J. M. Fritsch, 1992 : The role of the convective "trigger functions" in numerical forecasts of mesoscale convective systems. *Meteorol. Atmos. Phys.*, 49, 93-106.

_____ and _____, 1993 : Convective parameterization for mesoscale models : The Kain-Fritsch scheme. The representation of cumulus convection in numerical models. Meteor. Mono., 24, Amer. Meteor. Soc., 165-170.

Kanamitsu, M., 1989: Description of the NMC global data assimilation and forecast system. *Wea. and Forecasting*, 4, 335-342.

_____, and Coauthors, 1991: Recent changes implemented into the global forecast system at NMC. *Wea. and Forecasting*, 6, 425-435.

Kuo, Y.-H., R. Reed, and Y. Liu, 1996: The ERICA IOP 5 Storm. Part III: Mesoscale cyclogenesis and precipitation parameterization. *Mon. Wea. Rev.*, 1409-1434.

Lord, S. J. 1978: Development and observational verification of a cumulus cloud parameterization from the anvil clouds of deep tropical convection, University of California, Los Angeles, 359pp.

Mahrt, L. and H.-L. Pan, 1984 : A two layer model of soil hydrology. *Bound.-Layer Meteor.*, 29, 1-20.

Molinari, J. and M. Dudeck., 1986 : Implicit versus explicit convective heating in numerical weather prediction models. *Mon. Wea. Rev.*, 114, 1822-1831.

Pan, H.-L., 1990: A simple parameterization scheme of evapotranspiration over land for the NMC Medium-Range forecast model. *Mon. Wea. Rev.*, 118, 2500-2512.

_____ and W.-S. Wu, 1995 : Implementing a mass flux convective parameterization package for the NMC Medium-Range forecast model. *NMC office note 409*, [NOAA/NWS/NCEP, Environmental Modeling Center, WWB, Room 207, Washington DC 20233.]

_____ and L. Mahrt, 1987: Interaction between soil hydrology and boundary layer developments. *Boundary-Layer Meteor.*, 38, 185-202.

Rogers, R. and J. M. Fritsch, 1996: A general framework for convective trigger functions. *Mon. Wea. Rev.*, 124, 2438-2452.

Rogers, E., T. L. Black, D. G. Deaven, G. J. DiMego, Q. Zhao, M. Baldwin, N. W. Junker, and Y. Lin, 1996 : Changes to the operational "Early" Eta analysis/forecast system at the National Centers for Environmental Prediction. *Wea. and Forecasting*, 11, 391-413.

Stensrud, D.J., and J.M. Fritsch, 1994: Mesoscale convective systems in weakly forced large-scale environments. Part III : Numerical simulations and implications for operational forecasting. *Mon. Wea. Rev.*, 122, 2084-2104.

Zhang, D.-L., and R. Harvey, 1995 : Enhancement of extratropical cyclogenesis by a mesoscale convective system. *J. Atmos. Sci.,* 52, 1107-1127.

_____., J. S. Kain, J.M. Fritsch, and K. Gao, 1994: Comments on "Parameterization of convective precipitation in mesoscale numerical models: A critical review"., *Mon. Wea. Rev.*, 122, 2222-2231.

_____., E.-Y. Hsie, and M. W. Moncrieff, 1988 : A comparison of explicit and implicit predictions of convective and stratiform precipitating weather systems with a meso-β -scale numerical model. *Q. J. Royal Meteror. Soc.*, 114, 31-60.

Zhang, G. J. and N. A. McFarlane, 1991: Convective stabilization in midlatitudes. *Mon. Wea. Rev.,* 119, 1915-1928.

Ziegler, C.L., T. J. Lee, and R. A. Pielke, 1997 : Convective initiation at the dryline: A modeling study. *Mon. Wea. Rev.,* 125, 1001-1026.

Figure Lists

Fig. 1. Diurnal variation of the (a) scaled virtual temperature perturbation due to temperature (solid line) and moisture(dotted line) in (2), (b) PBL heights, and (c) wind speed at 10 m height level from the surface at the point "A", marked in Fig. 10a, obtained from the TR3M experiment with the new convective trigger in the cumulus convection scheme and prognostic cloud scheme for grid-resolvable physics.

Fig. 2. Surface analyses for (a) 1200 UTC 15, (b) 1200 UTC 16, and (c) 1200 UTC 17 May 1995. Areas of precipitation are indicated by shading. Tracks of well-defined low pressure areas are indicated by a chain of arrows ; locations of these centers at 6, 12, and 18 hours preceding map time are indicated by small white crosses in black squares.

Fig. 3. Analyzed 500 hPa geopotential height (solid lines), temperature (dotted lines), and wind vector for (a) 1200 UTC 15, (b) 1200 UTC 16, and (c) 1200 UTC 17 May 1995.

Fig. 4. Same as in Fig. 3, but for the 700 hPa level at 1200 UTC 16 May 1995.

Fig. 5. Analyzed 24-h accumulated rainfall (mm) ending at (a) 1200 UTC 16 and (b) 1200 UTC 17 May 1995. Values are box averages on the 25 km RSM grid from station data.

Fig. 6. Model domain and terrain distribution (contour intervals at 300 m). Interior box indicates the analysis domain for heavy precipitation in Figs. 5, 9, 10, and 11.

Fig. 7. 500 hPa temperature and geopotential height for the (a) 24-h and (b) 48-h forecasts from the TR3M experiment, valid at 1200 UTC 16 and 1200 UTC 17 May 1995, respectively.

Fig. 8. Difference of the 700 hPa temperature at the 24-h forecast valid at 1200 UTC 16 May 1995 from the OP3M and TR3M experiments(OP3M-TR3M).

Fig. 9. Predicted 24-h accumulated rainfall (mm) for the (a) 24-h and (b) 48-h forecasts, valid at 1200

UTC 16 and 1200 UTC 17 May 1995, respectively, from the OP1M, and the (c), and (d) from the TR1M experiment. Shaded areas and dotted lines denote the subgrid scale (implicit) and grid-resolvable (explicit) rain, respectively. Scales of the subgrid scale (implicit) rain are denoted as a bar below each figure.

Fig. 10. Same as in Fig. 9, but (a) and (b) from the OP3M, (c) and (d) from the TR3M, and (e) and (f) from the NOPT experiments, respectively. Letters A, B, and C in the figure designate the station points for temporal evolution anayses in section 5c.

Fig. 11. Domain-averaged, 6-h accumulated (a) total and (b) subgrid scale(implicit) rain, from the TR3M(solid lines), OP3M(dashed lines) and NOPT(dotted lines) experiments. Average is over the heavy precipitation region in the interior box of Fig. 6.

Fig. 12. (a) The temporal evolution of surface precipitation (mm h^{-1}) and (b) vertical profiles of the equivalent potential temperature, θ_e, (dotted lines) and saturated equivalent potential temperature, θ_{es}, (solid lines) at the point "A", marked in Fig. 10a, from the OP3M experiment. The profiles in (b) are constructed at 0400 UTC 16 May 1995.

Fig. 13. The temporal evolution of (a) surface precipitation (mm h^{-1}) and (c) vertical distribution of relative humidity (%) at the point "B", marked in Fig. 10a, from the TR3M experiment, and the corresponding forecasts, (b) and (d) from the OP3M experiment. Solid and dashed lines in (a) and (b) designate convective and grid-resolvable rain, respectively.

Fig. 14. Vertical profiles of the equivalent potential temperature, θ_e, (dotted lines) and saturated equivalent potential temperature, θ_{es}, (solid lines) at the point "B", marked in Fig. 10a, from the (a) TR3M experiment at 0548 UTC (thick lines) and 0748 UTC(thin lines), and from the (b) OP3M experiment at 0224 UTC(thick lines) and 0424 UTC(thin lines) May 16 1995.

Fig. 15. Same as in Fig. 13, but for the point "C" , marked in Fig. 10a.

Fig. 16. Same as in Fig. 14, but for the point "C" , marked in Fig. 10a, from the (a) TR3M experiment at 0400 UTC (thick lines) and 0500 UTC(thin lines), and from the (b) OP3M experiment at 0315 UTC(thick lines) and 0415 UTC(thin lines) May 16 1995.

Fig. 17. Vertical profiles of domain-averaged, time-averaged (a) temperature and (b) water vapor mixing ratio differences (OP3M- TR3M). Profiles are obtained from the data sets during the 48-h forecast over United States with 12 min. interval (every 6 time steps).

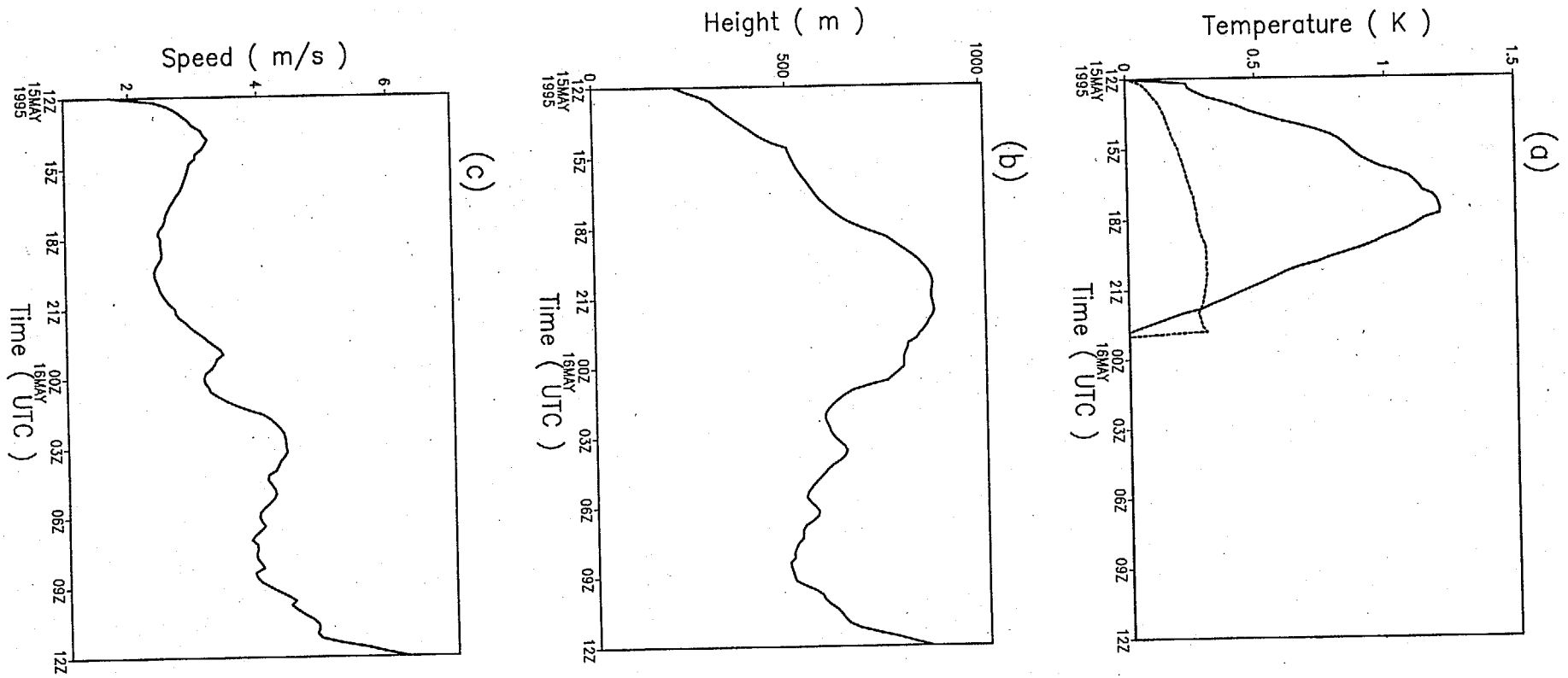

Fig. 1. Diurnal variation of the (a) scaled virtual temperature perturbation due to temperature (solid line) and moisture(dotted line) in (2), (b) PBL heights, and (c) wind speed at 10 m height level from the surface at the point "A", marked in Fig. 10a, obtained from the TR3M experiment with the new convective trigger in the cumulus convection scheme and prognostic cloud scheme for grid-resolvable physics.

Dec. 97

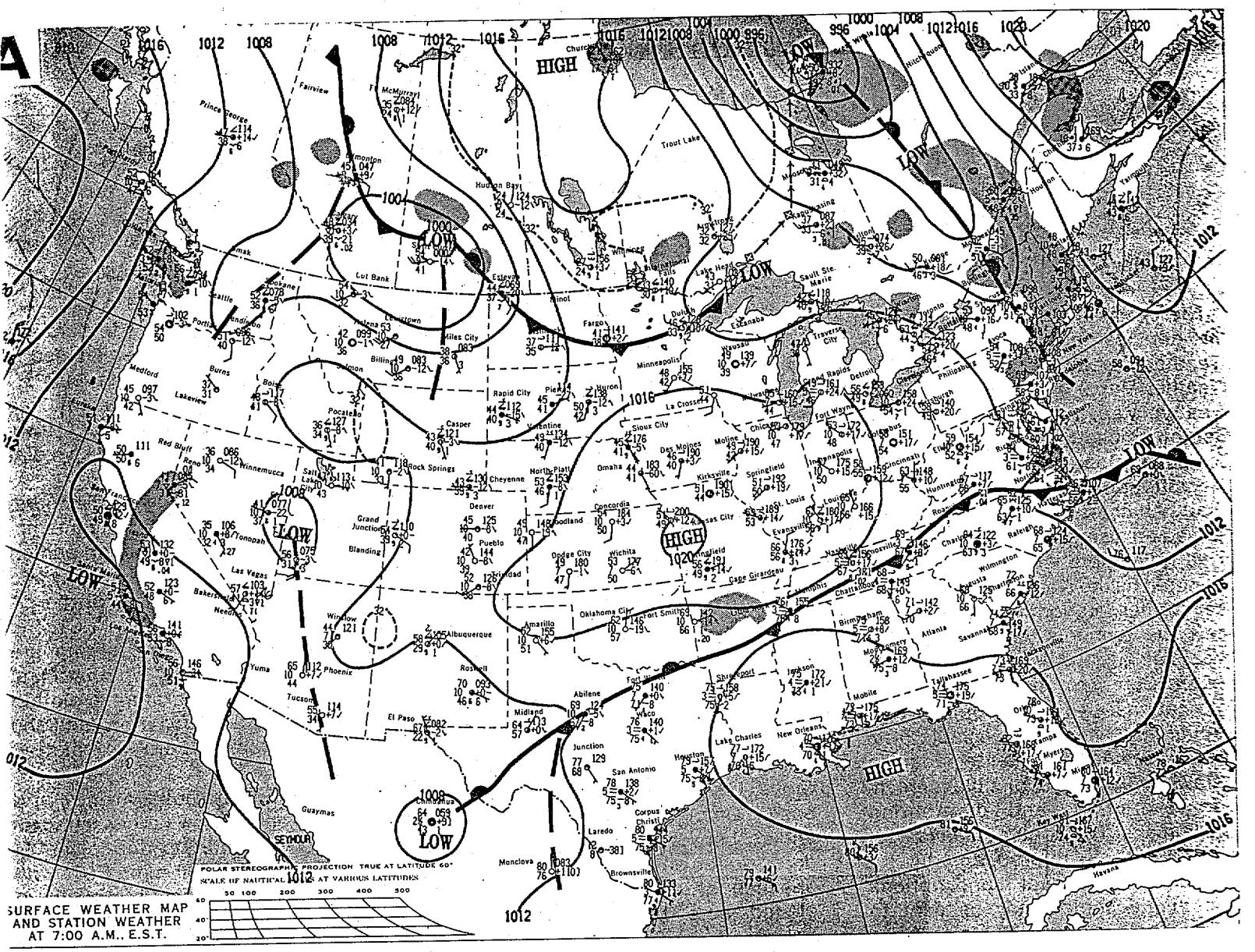

Fig. 2. Surface analyses for (a) 1200 UTC 15, (b) 1200 UTC 16, and (c) 1200 UTC 17 May 1995. Areas of precipitation are indicated by shading. Tracks of well-defined low pressure areas are indicated by a chain of arrows ; locations of these centers at 6, 12, and 18 hours preceding map time are indicated by small white crosses in black squares.

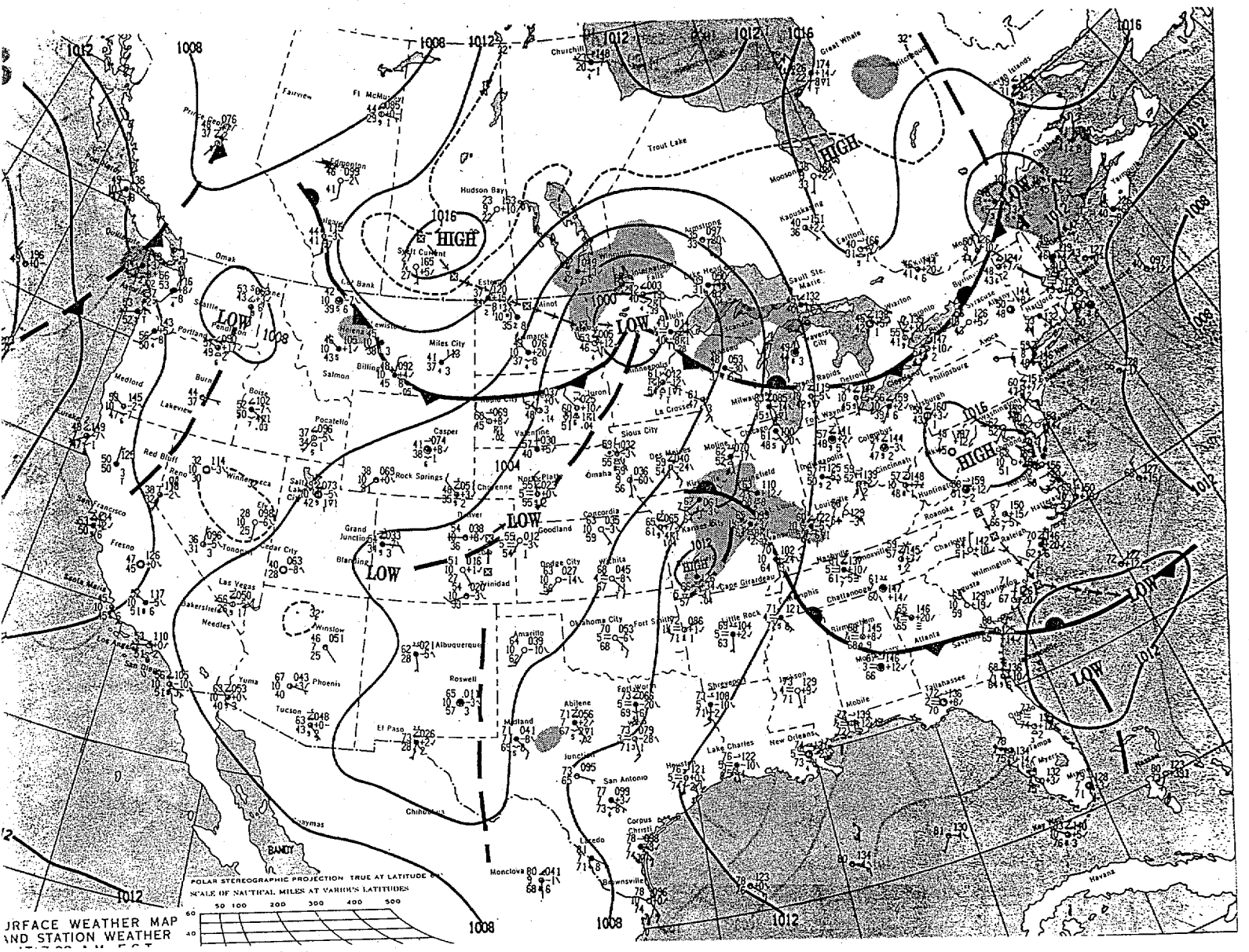

URFACE WEATHER MAP
ND STATION WEATHER

Fig. 2

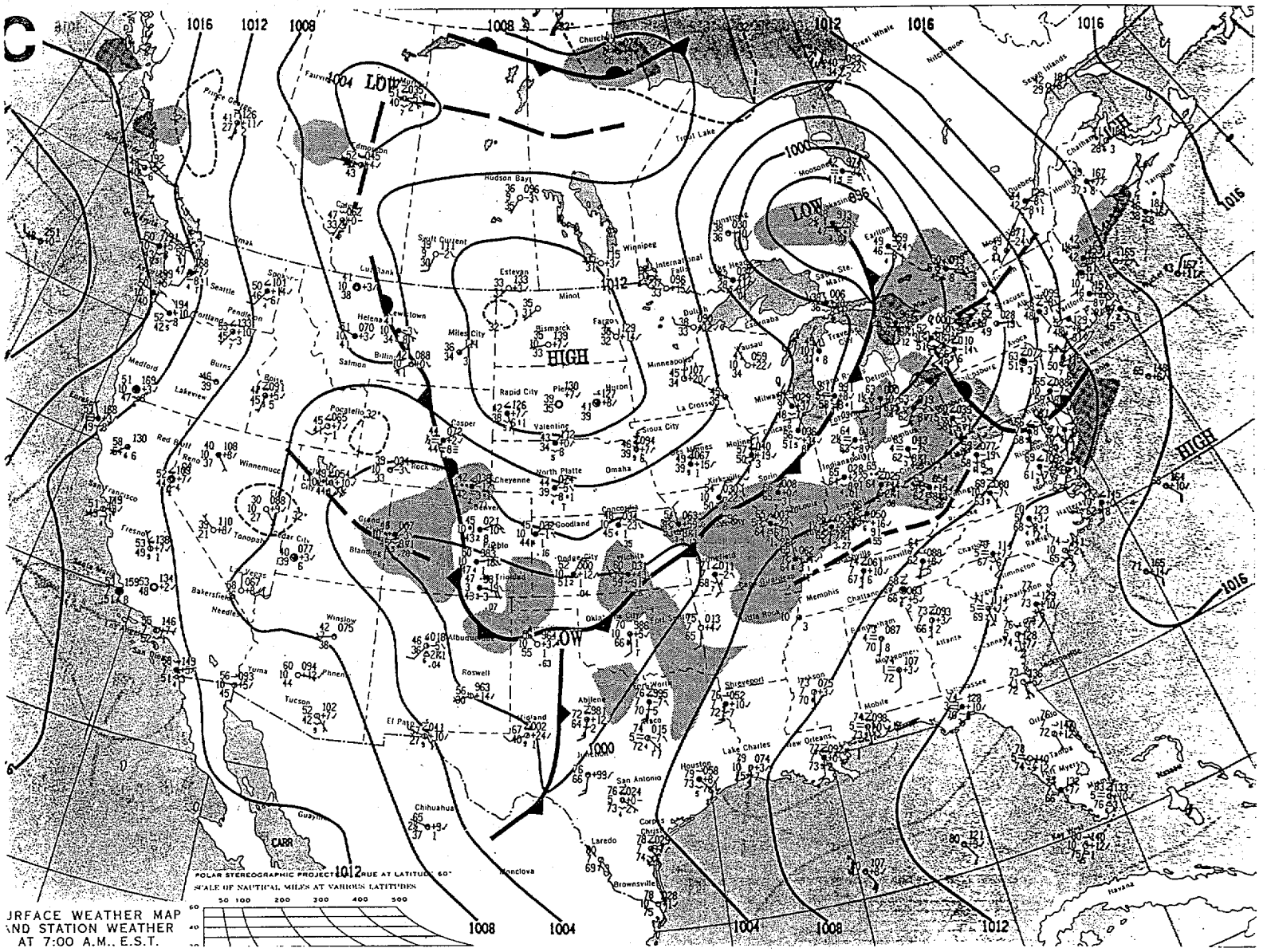

URFACE WEATHER MAP
ND STATION WEATHER
AT 7:00 A.M., E.S.T.

Fig. 2

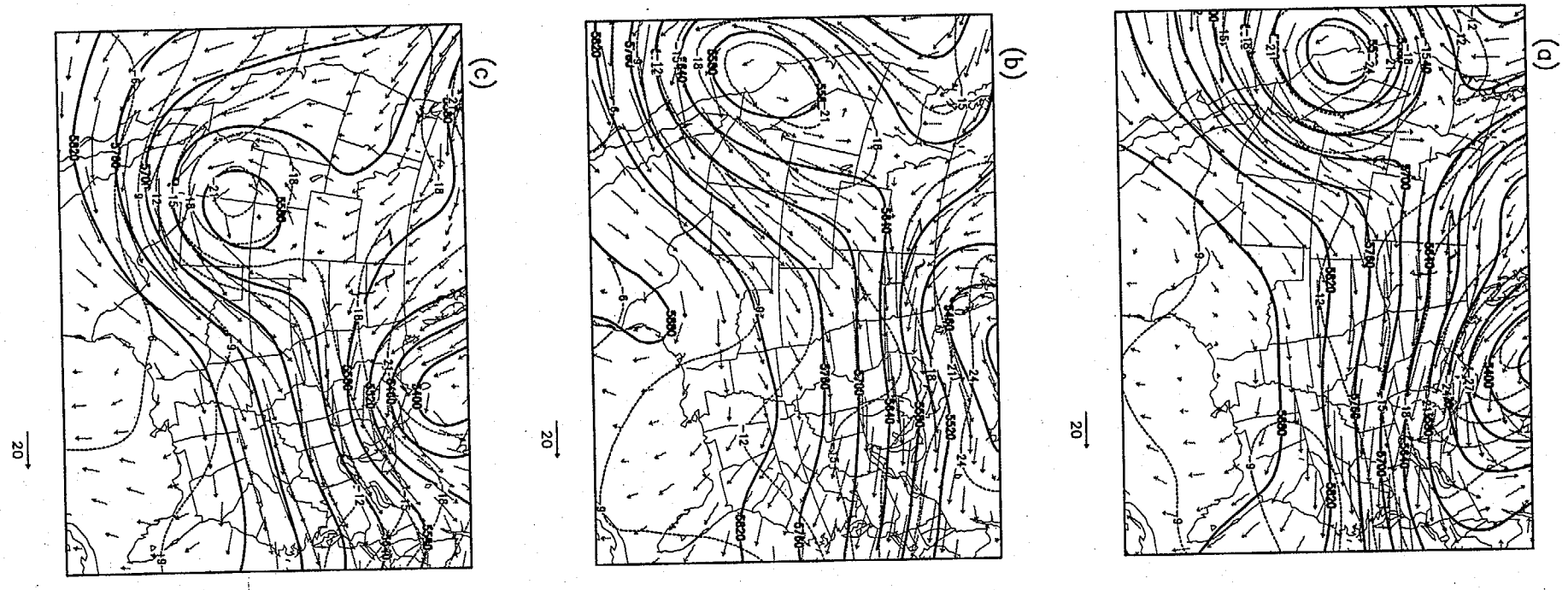

Fig. 3. Analyzed 500 hPa geopotential height (solid lines), temperature (dotted lines), and wind vector for (a) 1200 UTC 15, (b) 1200 UTC 16, and (c) 1200 UTC 17 May 1995.

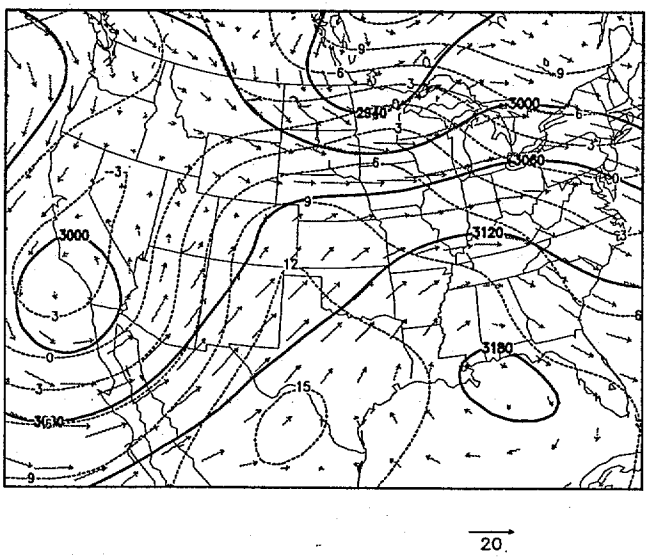

Fig. 4. Same as in Fig. 3, but for the 700 hPa level at 1200 UTC 16 May 1995.

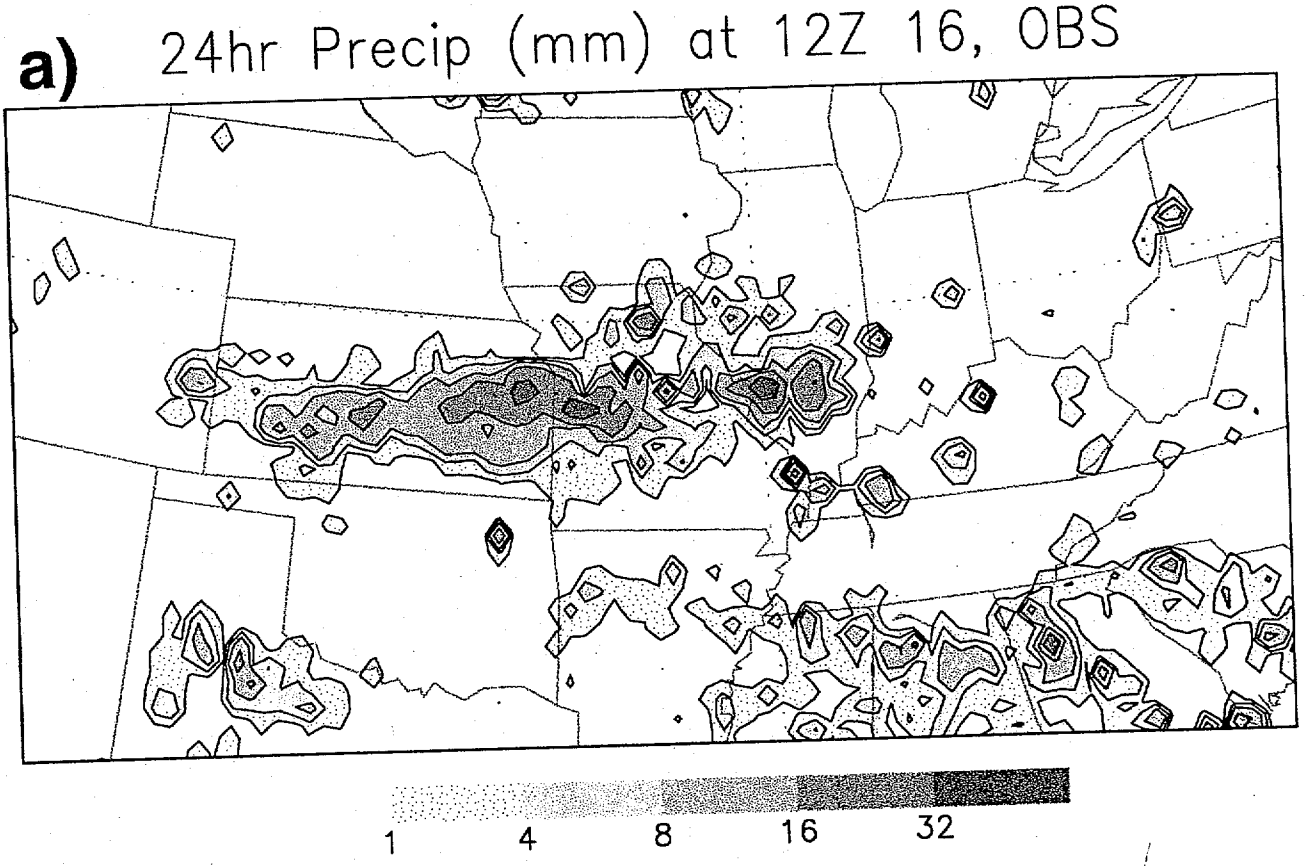

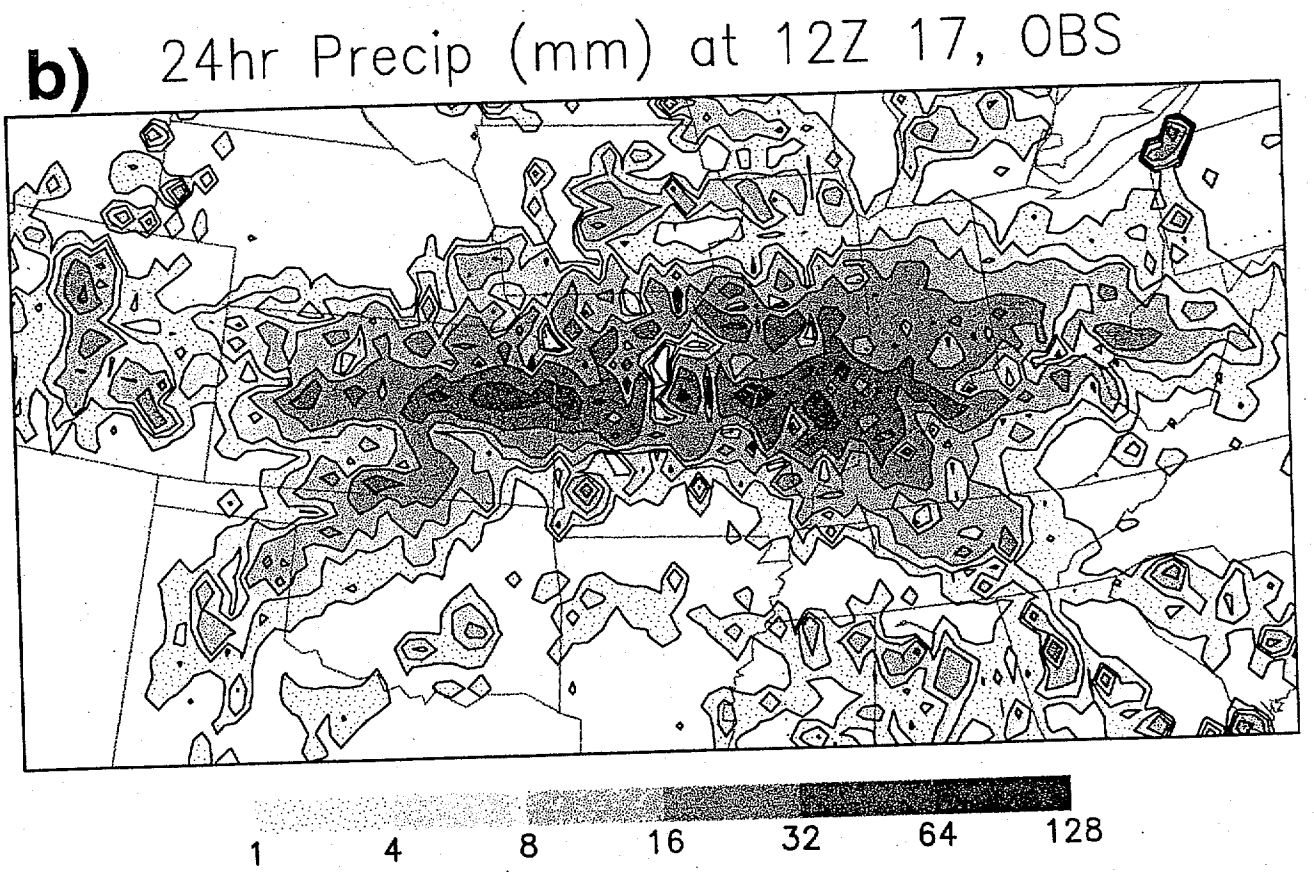

Fig. 5. Analyzed 24-h accumulated rainfall (mm) ending at (a) 1200 UTC 16 and (b) 1200 UTC 17 May 1995. Values are box averages on the 25 km RSM grid from station data.

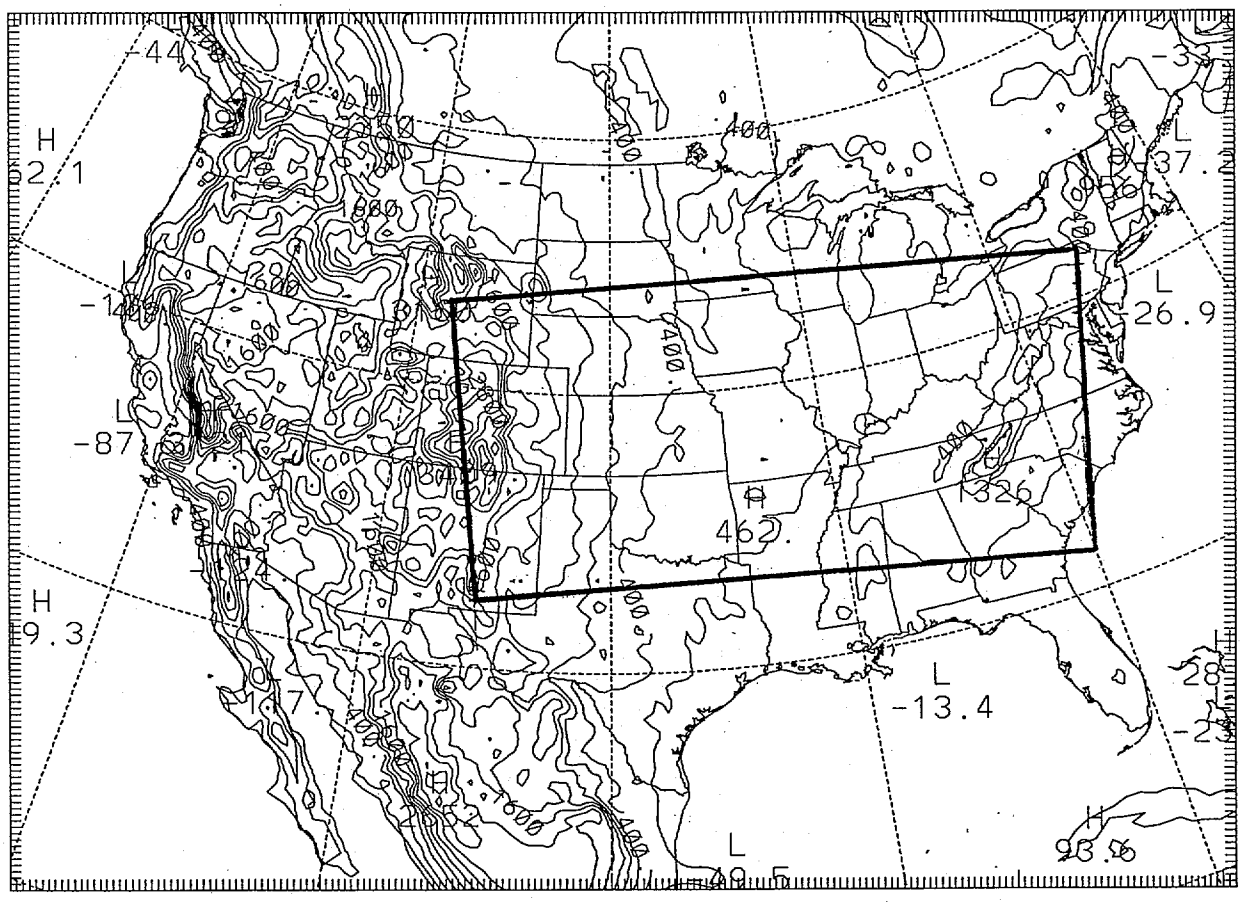

Fig. 6. Model domain and terrain distribution (contour intervals at 300 m). Interior box indicates the analysis domain for heavy precipitation in Figs. 5, 9, 10, and 11.

Fig. 6

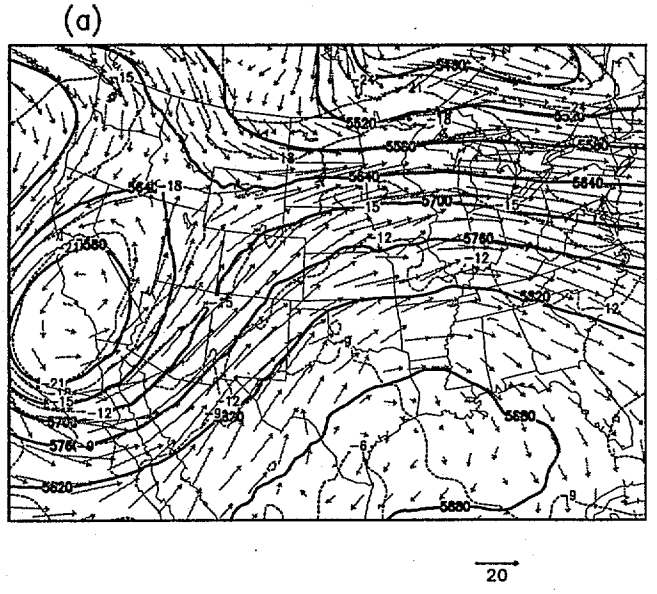

Fig. 7. 500 hPa temperature and geopotential height for the (a) 24-h and (b) 48-h forecasts from the TR3M experiment, valid at 1200 UTC 16 and 1200 UTC 17 May 1995, respectively.

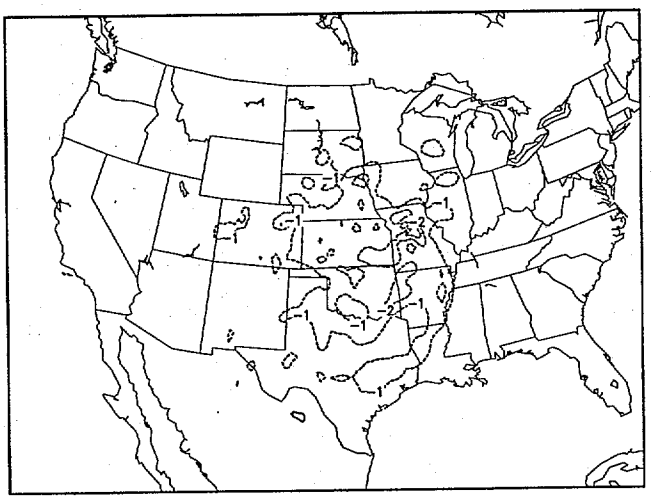

Fig. 8. Difference of the 700 hPa temperature at the 24-h forecast valid at 1200 UTC 16 May 1995 from the OP3M and TR3M experiments(OP3M-TR3M).

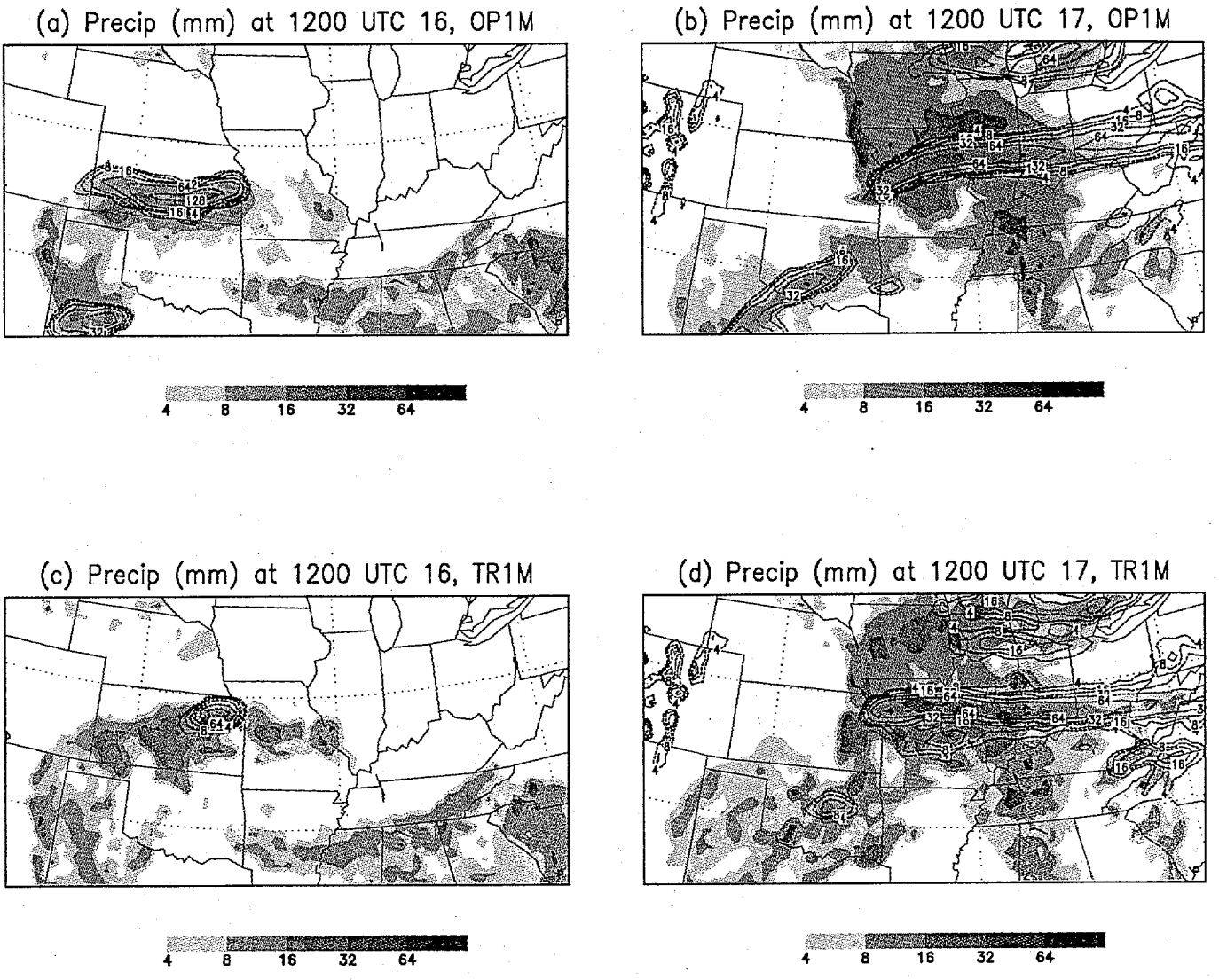

Fig. 9. Predicted 24-h accumulated rainfall (mm) for the (a) 24-h and (b) 48-h forecasts, valid at 1200 UTC 16 and 1200 UTC 17 May 1995, respectively, from the OP1M, and the (c), and (d) from the TR1M experiment. Shaded areas and dotted lines denote the subgrid scale (implicit) and grid-resolvable (explicit) rain, respectively. Scales of the subgrid scale (implicit) shaded areas are denoted as a bar below each figure.

Fig. 10. Same as in Fig. 9, but (a) and (b) from the OP3M, (c) and (d) from the TR3M, and (e) and (f) from the NOPT experiments, respectively. Letters A, B, and C in the figure designate the station points for temporal evolution anayses in section 5c.

(a) Precip (mm) at 1200 UTC 16, OP3M

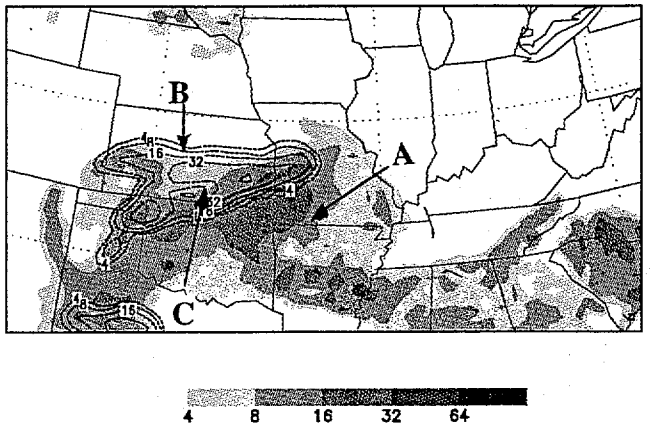

(b) Precip (mm) at 1200 UTC 17, OP3M

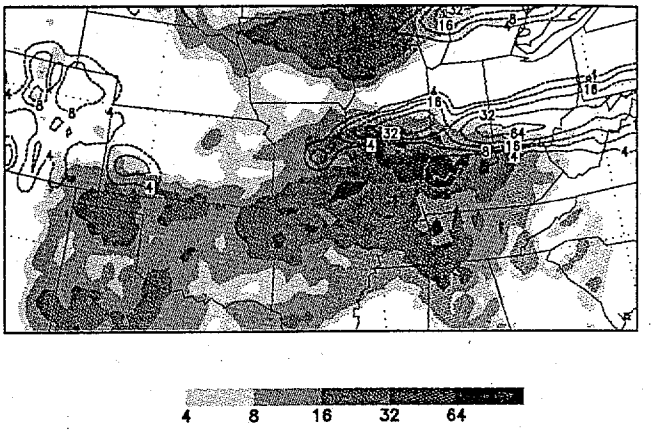

(c) Precip (mm) at 1200 UTC 16, TR3M

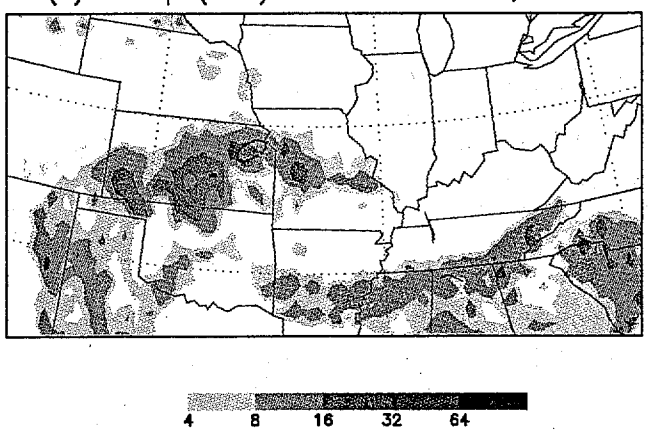

(d) Precip (mm) at 1200 UTC 17, TR3M

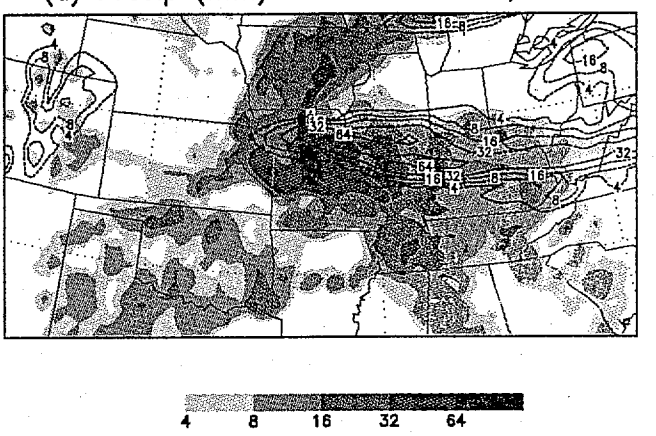

(e) Precip (mm) at 1200 UTC 16, NOPT

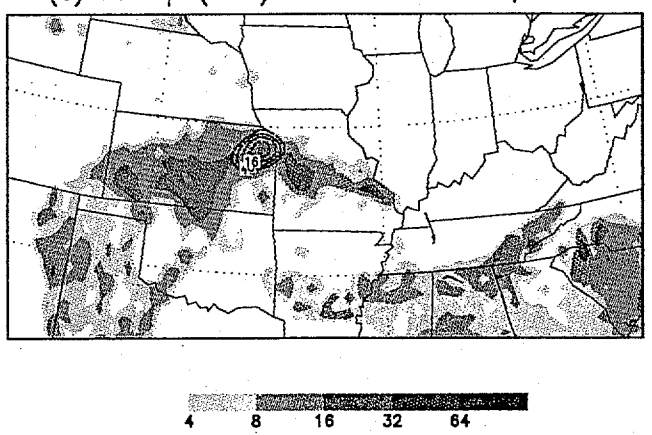

(f) Precip (mm) at 1200 UTC 17, NOPT

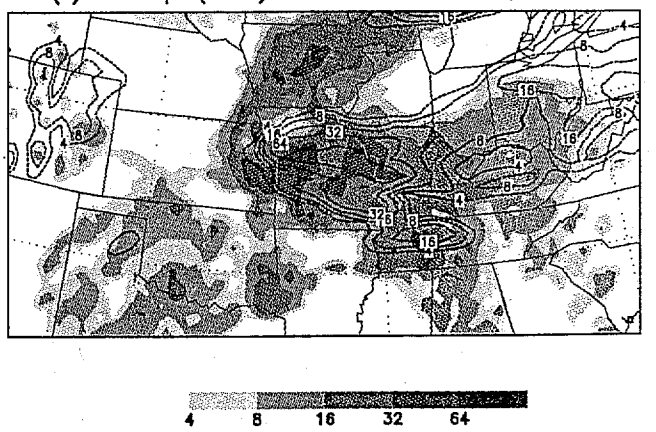

Fig. 10

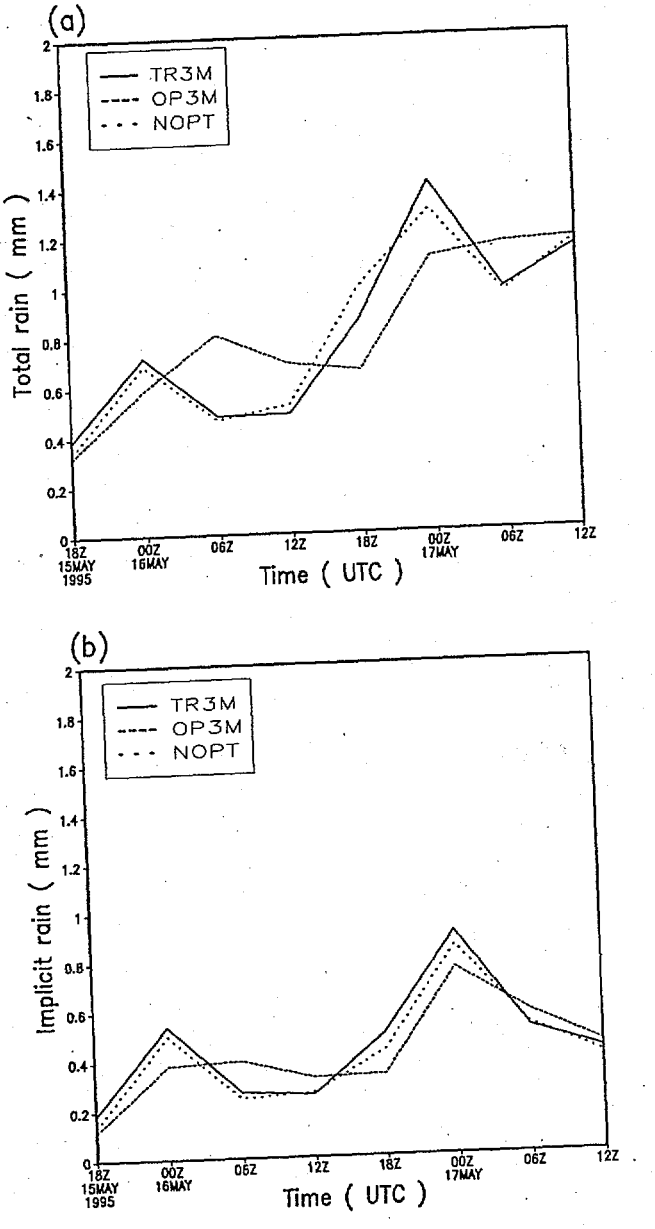

Fig. 11. Domain-averaged, 6-h accumulated (a) total and (b) subgrid scale(implicit) rain, from the TR3M(solid lines), OP3M(dashed lines) and NOPT(dotted lines) experiments. Average is over the heavy precipitation region in the interior box of Fig. 6.

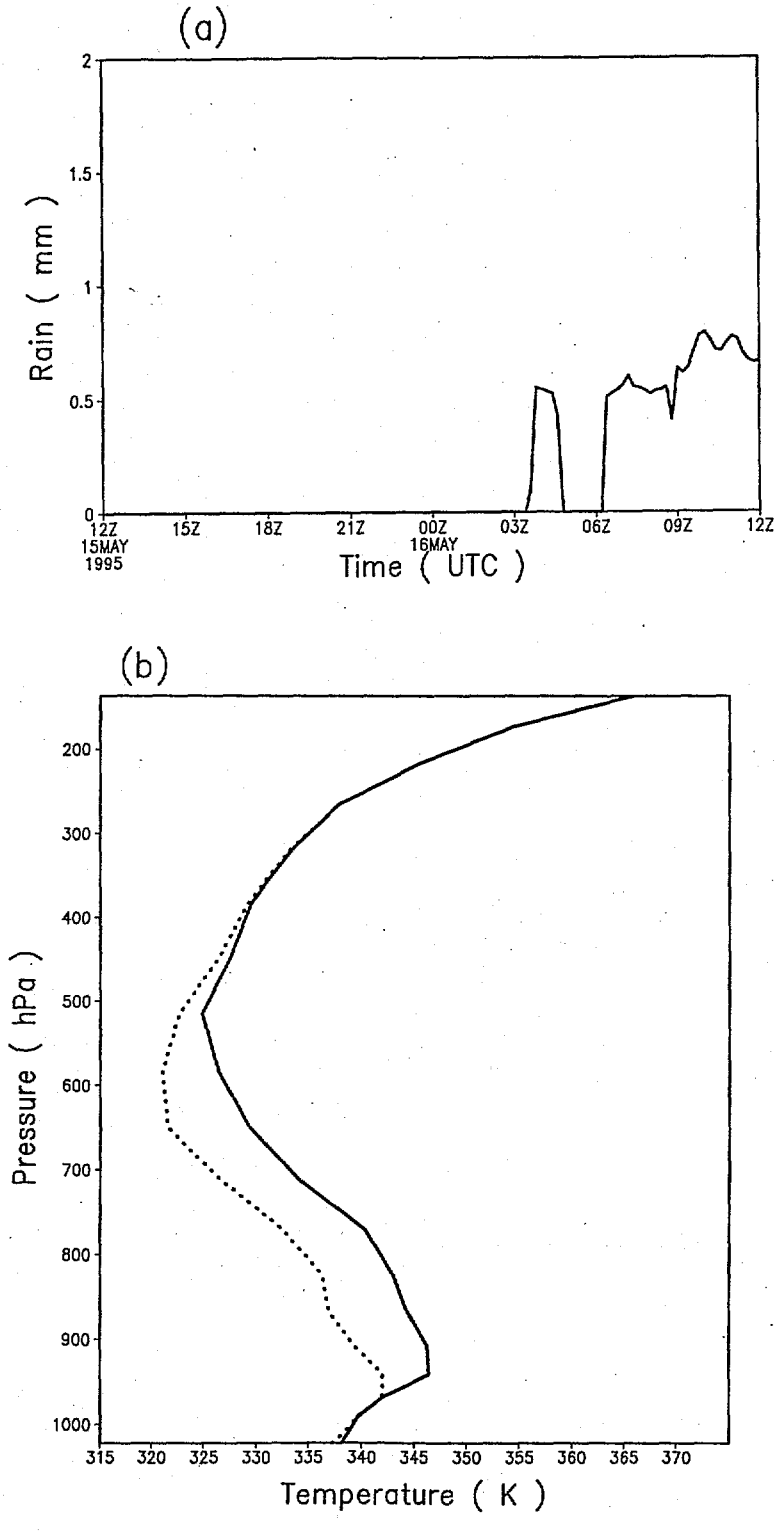

Fig. 12. (a) The temporal evolution of surface precipitation (mm h^{-1}) and (b) vertical profiles of the equivalent potential temperature, θ_e, (dotted lines) and saturated equivalent potential temperature, θ_{es}, (solid lines) at the point "A", marked in Fig. 10a, from the OP3M experiment. The profiles in (b) are constructed at 0400 UTC 16 May 1995.

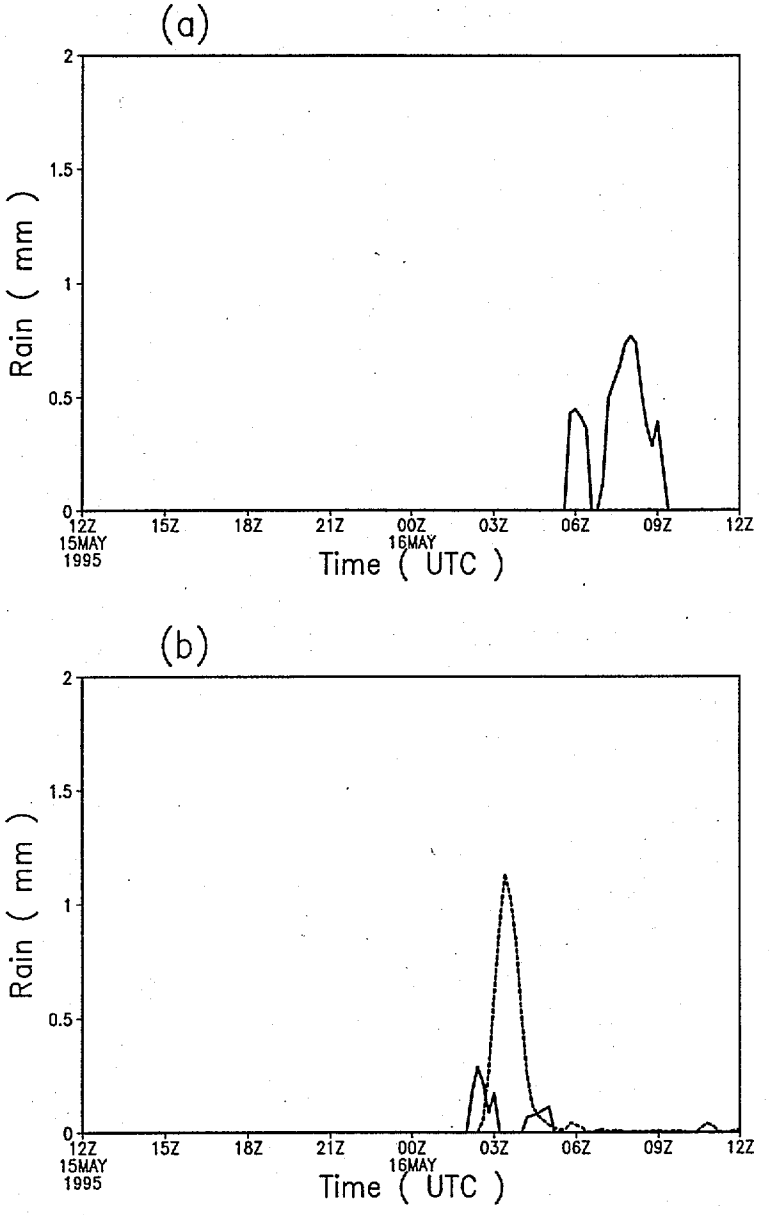

Fig. 13. The temporal evolution of (a) surface precipitation (mm h^{-1}) and (c) vertical distribution of relative humidity (%) at the point "B", marked in Fig. 10a, from the TR3M experiment, and the corresponding forecasts, (b) and (d) from the OP3M experiment. Solid and dashed lines in (a) and (b) designate convective and grid-resolvable rain, respectively.

(c)

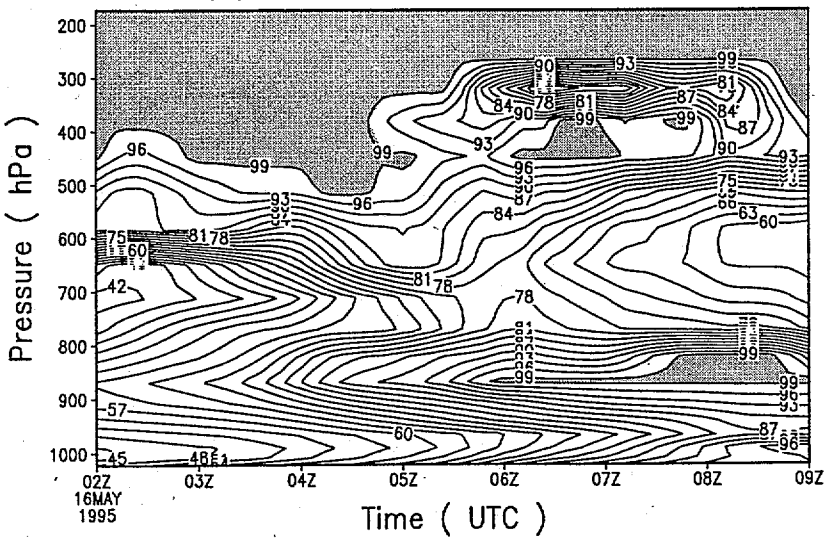
Pressure (hPa)
200
300
400
500
600
700
800
900
1000
02Z
16MAY
1995
03Z
04Z
05Z
06Z
07Z
08Z
09Z
Time (UTC)

(d)

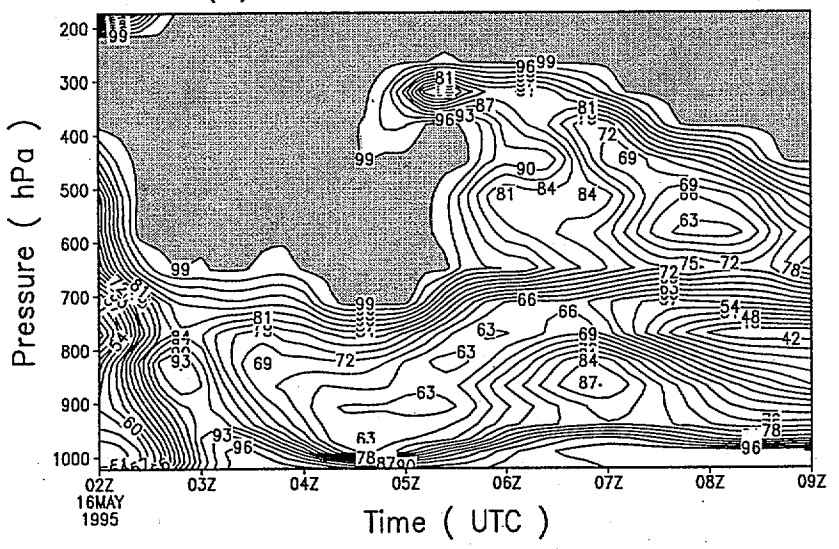
Pressure (hPa)
200
300
400
500
600
700
800
900
1000
02Z
16MAY
1995
03Z
04Z
05Z
06Z
07Z
08Z
09Z
Time (UTC)

Fig. 13

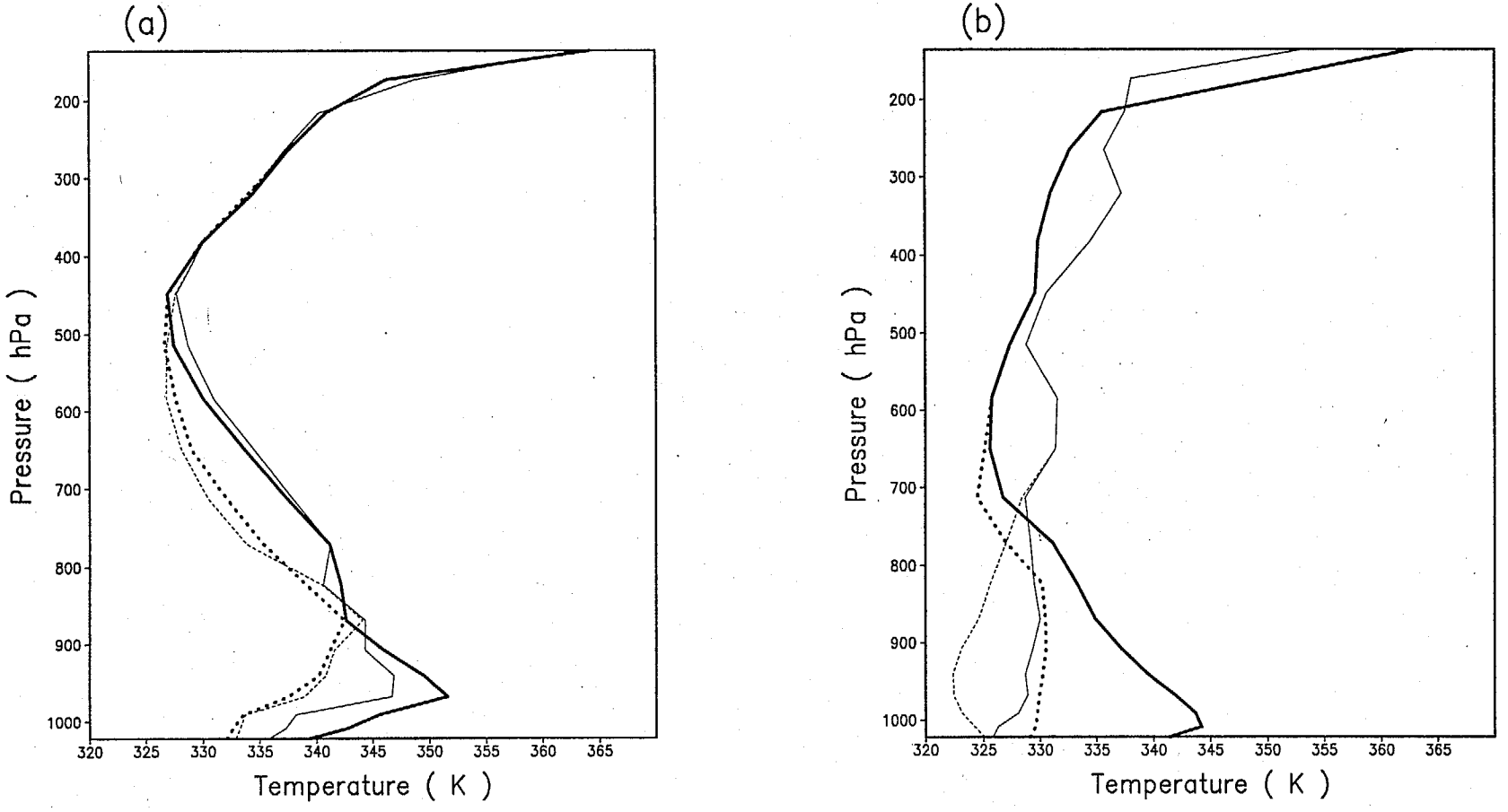

Fig. 14. Vertical profiles of the equivalent potential temperature, θ_e, (dotted lines) and saturated equivalent potential temperature, θ_{es}, (solid lines) at the point "B", marked in Fig. 10a, from the (a) TR3M experiment at 0548 UTC (thick lines) and 0748 UTC(thin lines), and from the (b) OP3M experiment at 0224 UTC(thick lines) and 0424 UTC(thin lines) May 16 1995.

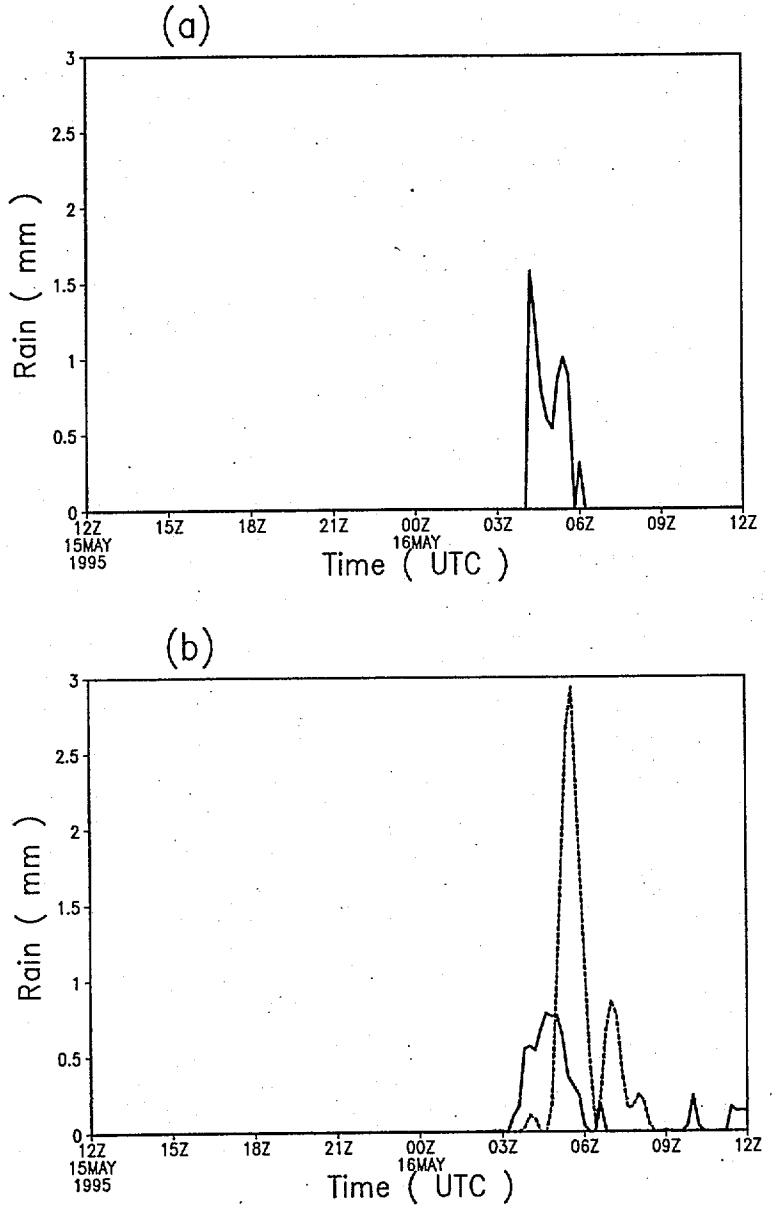

Fig. 15. Same as in Fig. 13, but for the point "C" , marked in Fig. 10a.

(c)

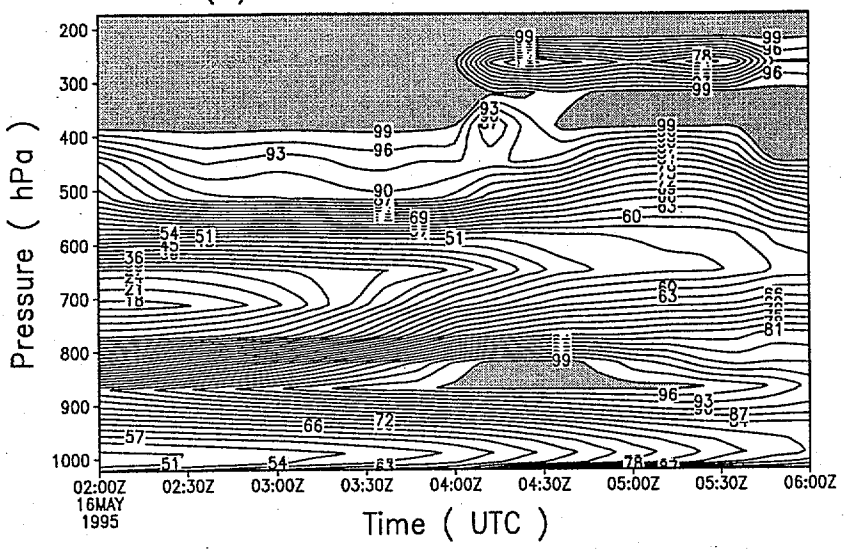
Pressure (hPa)
200
300
400
500
600
700
800
900
1000
02:00Z
16MAY
1995
02:30Z
03:00Z
03:30Z
04:00Z
04:30Z
05:00Z
05:30Z
06:00Z
Time (UTC)

(d)

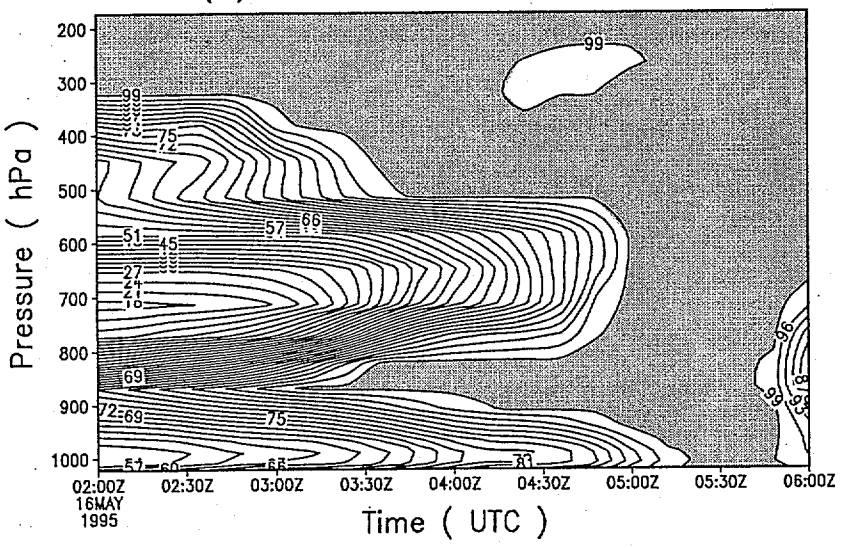
Pressure (hPa)
200
300
400
500
600
700
800
900
1000
02:00Z
16MAY
1995
02:30Z
03:00Z
03:30Z
04:00Z
04:30Z
05:00Z
05:30Z
06:00Z
Time (UTC)

Fig 15

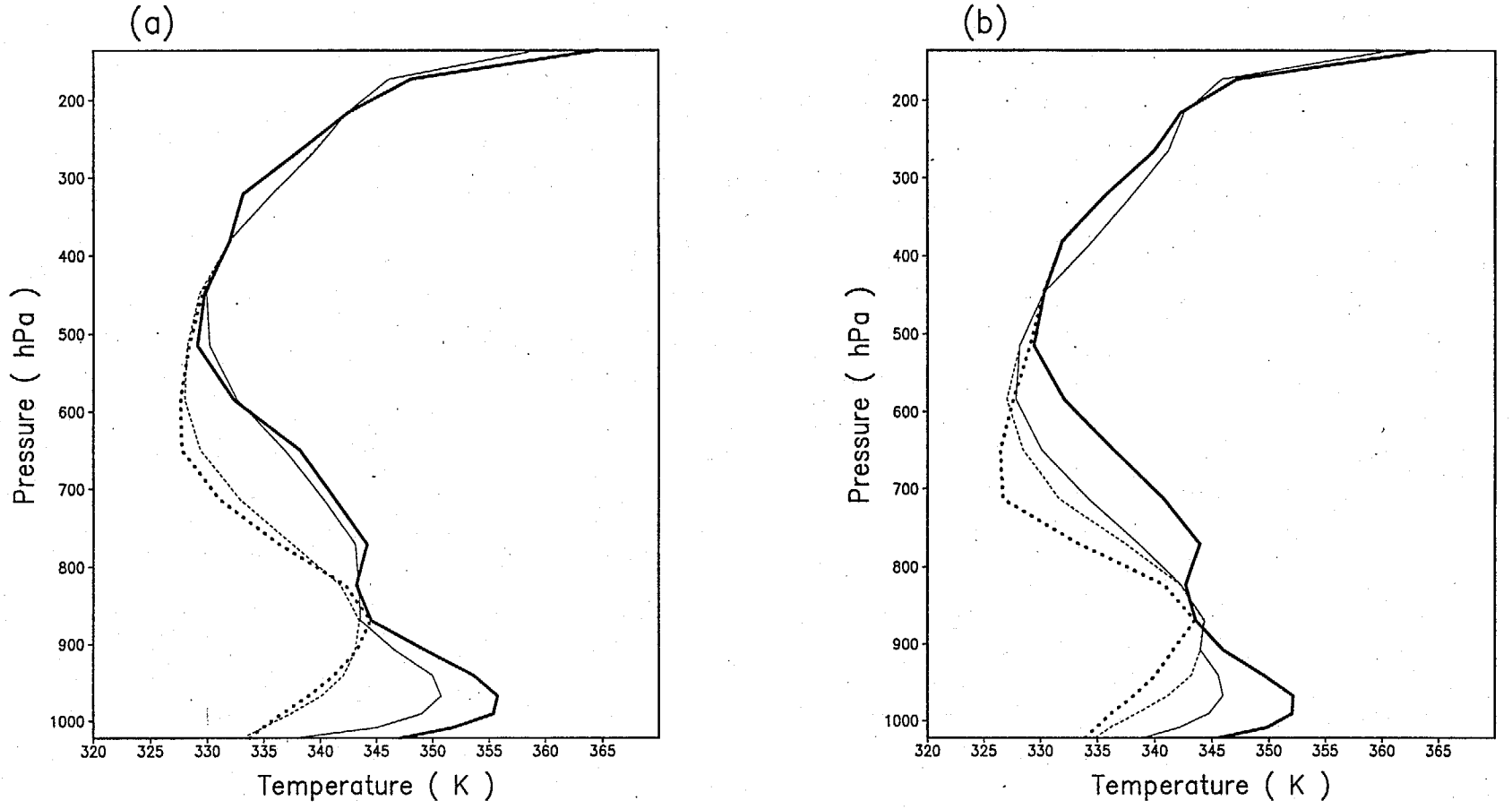

Fig. 16. Same as in Fig. 14, but for the point "C" , marked in Fig. 10a.

Fig. 17. Vertical profiles of domain-averaged, time-averaged (a) temperature and (b) water vapor mixing ratio differences (OP3M- TR3M). Profiles are obtained from the data sets during the 48-h forecast over United States with 12 min. interval (every 6 time steps).